A FINITE ELEMENT ANALYSIS OF FRACTURE TOUGHNESS OF $MoSi_2$/Nb AND NiAl/V COMPOSITES

A Thesis

Presented in Partial Fulfillment of the Requirements for

the Degree Master of Science in the

Graduate School of The Ohio State University

By

Rong Wang, M.S.

*****

The Ohio State University
1999

Approved by:

Master's Examination Committee:

Prof. Noriko Katsube, Co-advisor

Prof. Winston Soboyejo, Co-advisor

Noriko Katsube
Co-advisor

Winston Soboyejo
Co-advisor
Engineering Mechanics
Graduate Program

ABSTRACT

This study is divided roughly into two major parts. The first part of the study deals with the study of the toughening behavior of MoSi2 with reinforced Nb layers. The crack/microstructure interactions in layered MoSi2/Nb composites are presented. Toughening by crack bridging and blunting mechanisms will be modeled using micromechanics concepts. Finite element models for the prediction of interfacial debonding and mixed mode crack growth are also presented. It will highlight use of combined mechanics and materials approaches in the engineering of damage tolerant intermetallic matrix composites.

The second part of this work deals with the effect of vanadium layer thickness (100, 200 and 400 μm) on the resistance curve of NiAl/V microlaminates. The fracture resistance of the NiAl/V microlaminates modeled by finite element method is shown to increase with increasing layer thickness. The improved fracture toughness is associated with the crack bridging and the interactions of the crack with vanadium layers. The re-initiation of cracks in adjacent NiAl layer is also modeled by finite element methods. The re-initiation is shown to occur as a result of strain concentration at the interface between the adjacent NiAl layers and the vanadium layers. The initial deviation of the re-initiation crack from the pure mode I direction is shown to occur in the direction of maximum shear strain. Finally the finite element simulations match well with the experiment results.

Dedicated to my parents, wife and daughter

ACKNOWLEDGMENTS

I would like to thank all of my advisors for their help and encouragement throughout my graduate experience. I thank Prof. Noriko Katsube for her insightful suggestions on numerical modeling and on the mechanical meaning of the results. I thank Prof. Wolé Soboyejo for his help with all aspects of fracture toughness and his devotion to research.

I would like to thank Mingwei Li for his specimens and experiment results, and his helpful discussion of the modeling results.

I would like to acknowledge the support of the Division of Mechanics and Materials and the Division of Materials Research of the National Science Foundation for providing financial support for this study.

VITA

November 8, 1968	....	Born, Qingdao, China.
1986 – 1990	....	B.S. Department of Mechanics, Lanzhou University, China.
1990 – 1993	....	M.S. Department of Mechanics, Lanzhou University, China.
1997 – Present	....	Graduate Research Associate, Department of Aerospace Engineering, Applied Mechanics and Aviation, The Ohio State University.

PUBLICATIONS

1 Rong Wang, Fan Ye, Noriko Katsube and Wole Soboyejo, "The effect of layer thickness on crack propagation" Proceedings of the American Society of Mechanical Engineering Nov. 1997.

2. Rong Wang, Mingwei Li, Noriko Katsube and Wole Soboyejo, "An finite element analysis of the fracture behavior of layered NiAl/V composites"

3. Mingwei Li, Rong Wang, Noriko Katsube and Wole Soboyejo, "An investigation of the effects of layer thickness on the fracture behavior of layered NiAl/V composites", Mechanical Behavior of Advanced Materials, MD-Vol. 84 pp-317-323, 1998.

4. Mingwei Li, Rong Wang, Noriko Katsube and Wole Soboyejo, "An investigation of fracture behavior in layered NiAl/V composites", Acta Materialia / Scripta Materialia

FIELDS OF STUDY

Major Field: Engineering Mechanics

Studies in Fracture Mechanics, and Finite Element Analysis

TABLE OF CONTENTS

LIST OF TABLES

LIST OF FIGURES

CHAPTER 1

INTRODUCTION

High-temperature intermetallics are currently being developed for a range of structural aerospace applications [Gray et al., 1991, Vasudevan et al., 1992]. However, most intermetallics systems generally have low fracture toughness due to their limited number of slip systems [Aindow et al., 1991, Meschter, 1992]. There is, therefore, a need for research efforts designed to engineer improved fracture toughness in high-temperature intermetallic systems.

High-temperature intermetallics may be toughened by intrinsic modification (alloying/heat treatment) or extrinsic modification (composite approach) [Ritchie et al., 1985]. Multiple toughening mechanisms may also be used to engineer fracture toughness improvements that are significantly greater than the matrix toughness levels. However, the engineering of such improvements requires a detailed understanding of the stress states and shielding mechanisms that can occur under potential service conditions.

Recent work [Soboyejo et al., 1996], has shown that layered composites with improved fracture toughness (~20 $MPa\sqrt{m}$) may be engineered by ductile phase toughening (crack bridging and crack-tip blunting). However, the influence of composite stress states on crack initiation/growth is not fully understood. There is, therefore, a need for detailed studies of the effects of layer geometry on crack growth.

This study presents the results of a computational study of crack growth and toughening in a layered MoSi2/Nb composite and Nial/V composite with the comparison of experiments. The stress states and crack driving forces associated with bridged/unbridged mode I cracks are computed using analytical and finite element methods, also the Residence curves for Nial/V composites with three distinct layers of are calculated. The shielding contributions from crack bridging and crack-tip blunting are also quantified using micro-mechanics approaches. The numerical predictions of crack re-initiation sites and propagation directions match those with the experimental data. The critical loads, where a crack reinitiates at the other side of the vanadium layer and propagates to the next vanadium layer, are numerically predicted and compared against experimental data. The effect of thickness on the R-curve behavior is examined.

CHAPTER 2

FUNDAMENTALS OF FRACTURE AND FINITE ELEMENT METHOD

2.1 Fundamentals of Fracture Mechanics

2.1.1 INTRODUCTION

In this chapter, the basic concepts in the fields of fracture mechanics and finite element method which are relevant to the present study are reviewed. The concept of strain energy release rate, G, is first presented as an introduction to the subject of Linear Elastic Fracture Mechanics (LEFM). In the framework of LEFM, several important topics are introduced. The elastic crack tip stress field and the concept of stress intensity factor, K, are presented. The Von Mises stress criterion and the concept of the J-integral are discussed, and the relationship between G, K, and J is presented. Also the finite element method for elastic and plastic material to deal with the stress singularity at the crack tip of the specimen are discussed.

2.1.2 STRAIN ENERGY RELEASE RATE

The concept of strain energy release rate, G, is one of the most fundamental in the understanding of fracture. The strain energy release rate is defined as the rate of decrease of the total potential energy, Π, of a system with respect to crack length, a (per unit thickness of the crack front):

$$G = -\frac{d\Pi}{da} \tag{2.1}$$

G represents the elastic energy per unit crack surface area that is available for infinitesimal crack extension [Ewalds, 1984], and can be thought of as a driving force for crack extension. From the works of Griffith [Griffith, 1921] and Irwin [Irwin, 1948], the following relationship can be derived:

$$G = 2(\gamma_e + \gamma_p) \tag{2.2}$$

where γ_e is the elastic surface energy of the material and γ_p is the plastic strain work from crack extension. Equation 2.2 indicates that a crack will extend if G reaches a critical value, G_c, equal to the energy required to create the new crack surfaces and the plastic zone. G_c can be considered as a material parameter and is a measure of the intrinsic resistance of a material to crack growth.

2.1.3 LINEAR ELASTIC FRACTURE MECHANICS (LEFM)

There are three different modes of loading that can cause stresses to develop at a crack tip, as illustrated in Figure 2.1.

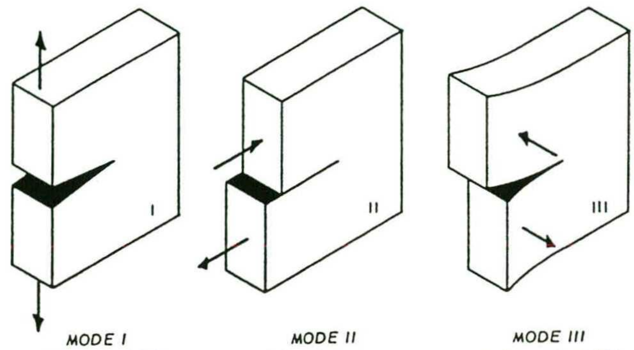

Figure 2.1 The three modes of crack-tip loading [Ewalds, 1984]

Mode I loading is also called the opening mode, where the crack surfaces move directly apart from each other. Mode II loading is called the sliding mode or in-plane shearing mode, where the crack surfaces move over one another in a direction perpendicular to the crack front. Mode III loading is called the tearing mode, or anti-plane shearing mode, where the crack surfaces move in directions parallel to the crack front.

Irwin [Irwin, 1957], using the complex variable method developed by Westergaard [Westergaard, 1939], quantified the near-tip stress fields surrounding a linear elastic crack as

$$\sigma_{ij} = \frac{K}{\sqrt{2\pi r}} f_{ij}(\theta) + O_{ij}\left(r^{1/2}\right) + \ ..... \tag{2.3}$$

where σ_{ij} is the stress tensor, K is the stress intensity factor, r is the radial distance from the crack-tip, and θ is the angle between the crack propagation direction and a vector parallel to r, as shown in Figure 2.2.

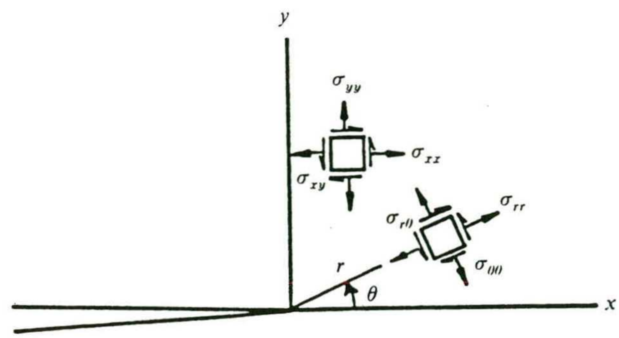

Figure 2.2 Coordinate system and stresses near the tip of a crack [Suresh, 1991]

In the vicinity of the crack tip, the higher order terms, symbolized as O(r) in Equation (2.3), can be neglected because they vanish as r approaches zero [Suresh, 1991]. The stress intensity factor is the fundamental parameter used in linear elastic fracture mechanics. This parameter K is a measure of the strength, or intensity, of the crack-tip stress fields. For an infinite plate, K can be expressed as [Broek, 1982]:

$$K = \sigma_a \sqrt{\pi a} \tag{2.4}$$

where σ_a is the remote applied stress and 'a' is the crack length. The expression for K changes when solutions for stresses in finite size specimens are needed. In the case of finite sized specimens,

$$K = Y\sigma_a \sqrt{\pi a} \tag{2.5}$$

where Y is a geometric factor that is dependent on specimen dimensions. As discussed earlier, there are three modes of loading that can cause stresses at the crack-tip. Normal stresses that are caused by Mode I loading are characterized by the Mode I stress intensity factor K_I. Likewise, shear stresses, caused by Mode II or Mode III loading, are characterized by K_{II} or K_{III}, respectively. A body that is loaded arbitrarily could experience mixed-mode loading, meaning that more than one of the three loading modes would be present. The elastic near-tip stress field in a body which is experiencing mixed-mode loading can be calculated by using the method of superposition and adding together the stresses caused by each mode.

Both the strain energy release rate, G, and the stress intensity factor, K, can be thought of as being driving forces for crack extension. For a general three-dimensional case, or the case of a two-dimensional plane strain state involving both in-plane and out-of-plane loading, these two parameters are related by [Suresh, 1991]

$$G = \frac{(1-\nu^2)}{E}\left(K_I^2 + K_{II}^2\right) + \frac{(1+\nu)}{E}K_{III}^2 \quad . \tag{2.6}$$

where E is the elastic modulus of the material and ν is the Poisson's ratio.

For the case of plane stress state, this expression reduces to

$$G = \frac{1}{E}\left(K_I^2 + K_{II}^2\right) \tag{2.7}$$

Plane stress and plane strain will be discussed shortly.

The expression for stress in terms of K, Equation (2.3), when the higher order terms are neglected, is only valid within a small region around the crack-tip. This is due to the fact that the higher order terms O(r) may not be neglected at large r. The region where these higher order terms O(r) may be neglected, and the stresses may be expressed solely in terms of K, is called the region of K-dominance [Kanninen, 1985]. These stresses are also sometimes called K-fields. Due to the singular nature of the elastic stress field, Equation (2.3) says that the stresses at the crack tip approach infinity as the radius r approaches zero. Physically, in a real material, this does not occur since some sort of inelastic or plastic deformation will take place at the crack-tip to relax the high stresses. Figure 2.3 shows a schematic of the region of K-dominance around a crack-tip, denoted by the radius D, and also the region immediately surrounding the crack-tip where inelastic deformation has occurred, represented by the radius R. The K-fields can be used to characterize the stress state at a crack-tip as long as the region of inelastic deformation is confined well within the region of K-dominance [Suresh, 1991], and is sufficiently small compared to other characteristic geometric dimensions such as plate thickness. When this is the case, it is said that small-scale yielding conditions are satisfied and that small-scale yielding is taking place.

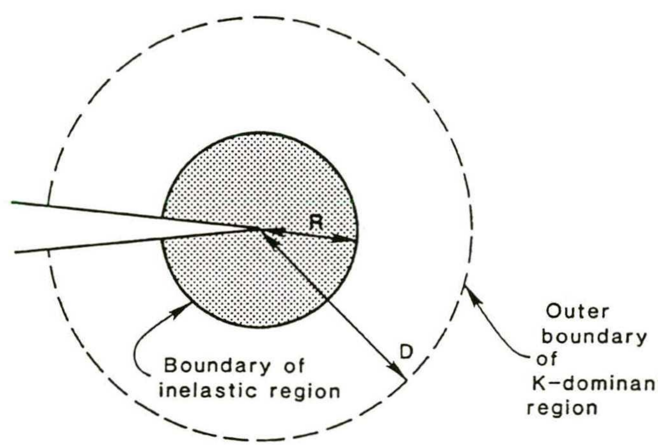

Figure 2.3 The region of K-dominance at a crack-tip under small-scale yielding [Kanninen, 1985]

In ductile materials, such as metals, this region of inelastic deformation is caused by plastic deformation at the crack-tip and is called the plastic zone. The size and the shape of the plastic zone depend on the stress states at the crack-tip.

The shape of the crack-tip plastic zone can be approximated in a purely LEFM analysis by use of the Von Mises yield criterion which states that yielding will occur when

$$(\sigma_1-\sigma_2)^2+(\sigma_2-\sigma_3)^2+(\sigma_3-\sigma_1)^2=2\sigma_{ys}{}^2 \tag{2.8}$$

where σ_1, σ_2 , and σ_3 are the principal stresses and σ_{ys} is the uniaxial yield stress. From this criterion, the radius of the plastic zone as a function of θ (same θ as in Figure 2.2) can be expresses as [Gdoutos, 1993]:

$$\begin{aligned}
&\text{Plane strain:} \quad r_p(\theta)=\frac{K_I^2}{4\pi\sigma_{ys}{}^2}\left[\frac{3}{2}\sin^2(\theta)+(1-2\nu)^2(1+\cos\theta)\right] \\
&\text{Plane stress:} \quad r_p(\theta)=\frac{K_I^2}{4\pi\sigma_{ys}{}^2}\left[1+\frac{3}{2}\sin^2(\theta)+\cos\theta\right]
\end{aligned} \tag{2.9}$$

Figure 2.4 shows the difference between the plastic zones predicted by the Von Mises yield criterion for plane stress and plane strain stress states.

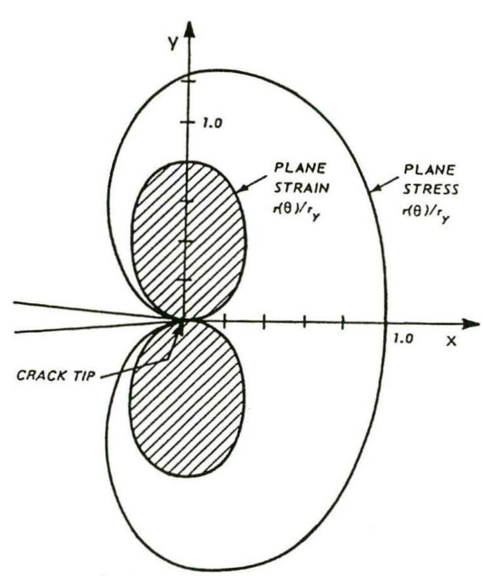

Figure 2.4 Plastic zone shapes predicted by the Von Mises yield criterion [Ewald, 1984]

As discussed, the state of stress at a crack-tip in a very thin specimen may be idealized as being plane stress, while the stress states in a thick specimen may be considered plane strain.

Under small-scale yielding conditions, the stress intensity factor, K, gives a unique characterization of the near-tip stress fields. However, when the plastic zone gets too large for small-scale yielding to apply, K is no longer valid. The parameter which corresponds to K can be used for the characterization of monotonic, nonlinear fracture is the J-integral proposed by Rice [Rice, 1968]. The J-integral is a line-integral following any arbitrary contour encircling the crack-tip and is defined as

$$J = \int_{\Gamma} \left(w\,dy - \mathbf{T} \cdot \frac{\partial \mathbf{u}}{\partial x} ds \right) \tag{2.10}$$

where w is the strain energy density of the material, y is the distance along the direction normal to the plane of the crack, **T** is the traction vector, **u** is the displacement vector, and s is the arc length along the contour Γ. For materials undergoing linear elastic or nonlinear elastic deformation, J is independent of the path Γ around the crack-tip. The J-integral has been shown [Rice, 1968] to be equal to the rate of decrease of the potential energy with respect to the crack length (per unit thickness):

$$J = -\frac{d\Pi}{da} \tag{2.11}$$

Therefore, for linear elastic materials, the J-integral and the strain energy release rate, G, are equivalent.

$$J = G = \frac{\left(1-\nu^2\right)}{E}\left(K_I^2 + K_{II}^2\right) + \frac{\left(1+\nu\right)}{E}K_{III}^2 \qquad \text{(Plane strain or three-dimensional)}$$

$$J = G = \frac{1}{E}\left(K_I^2 + K_{II}^2\right) \qquad \text{(Plane stress)} \tag{2.12}$$

Just like G and K, the J-integral can be thought of as a crack driving force. When the plastic zone size becomes too large for small-scale yielding and Linear Elastic Fracture Mechanics to apply, J becomes the needed parameter of interest in the characterization of such nonlinear fracture. Under these conditions, the methodologies of Elastic-Plastic Fracture Mechanics apply.

2.2 Theoretical Background of Singularity Crack-Tip Finite Elements

2.2.1 INTRODUCTION

The finite element method (FEM) is a very powerful tool that can be used to easily calculate stresses, strains, and deformations in structures, no matter how complicated the shape. However, when a component has a crack present, with the associated stress and strain singularities discussed above, conventional elements must be modified to exhibit these singularities. Barsoum, and also Henshell and Shaw, showed that 8-noded isoparametric elements can be used for plane stress and plane strain fracture mechanics analyses where a crack is present [Barsoum, 1976; Henshell and Shaw, 1975]. It was shown that the required $\frac{1}{\sqrt{r}}$ linear elastic stress and strain singularities for crack-tip stress fields can be achieved by placing the mid-side nodes near the crack-tip at the 1/4 position instead of the 1/2 position. Barsoum also showed that triangular elements (2-D) formed by collapsing one side of the element into the crack-tip, produced much more accurate results (for stress intensity factors) than the rectangular 2-D elements. A recount of the derivation by Barsoum for the 8-noded isoparametric element is presented here for completeness [Barsoum, 1977].

2.2.2 SINGULARITY CRACK-TIP ELEMENT

The geometry of an 8-noded plane isoparametric element is mapped into the normalized region in ξ-η space ($-1 \leq \xi \leq 1$, $-1 \leq \eta \leq 1$) through the transformations

$$x=\sum_{i=1}^{8} N_i(\xi,\eta)x_i$$

$$y=\sum_{i=1}^{8} N_i(\xi,\eta)y_i \tag{2.13}$$

$$N_i(\xi,\eta)=\begin{array}{l}\frac{1}{4}\left[(1+\xi\xi_i)(1+\eta\eta_i)-(1-\xi^2)(1+\eta\eta_i)-(1-\eta^2)(1+\xi\xi_i)\right]\xi_i^2\eta_i^2 \\ +\frac{1}{2}(1-\xi^2)(1+\eta\eta_i)(1-\xi_i^2)\eta_i^2+\frac{1}{2}(1-\eta^2)(1+\xi\xi_i)(1-\eta_i^2)\xi_i^2\end{array} \tag{2.14}$$

where (x_i, y_i) are the coordinates of node i in x-y space, and (ξ_i, η_i) are the nodal coordinates in ξ-η space. Figure 2.5 shows the geometry of an 8-noded isoparametric element and its transformation into ξ-η space.

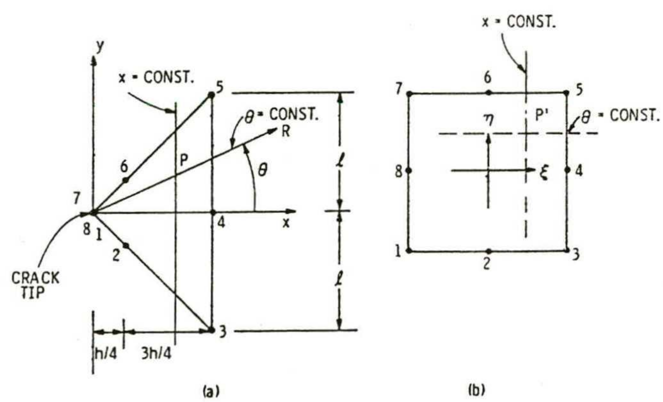

Figure 2.5 8-noded isoparametric element in geometrical x-y space and its transformation into ξ-η space [Barsoum, 1977]

As can be seen for the element shown in Figure 4.1, the geometric coordinates of the nodes are

$$x_1=x_7=x_8=0\ ,\ x_2=x_6=\frac{h}{4}\ ,\ x_3=x_4=x_5=h$$

and (2.15)

$$y_1=y_7=y_8=y_4=0\ ,\ y_2=-y_6=-\frac{\ell}{4}\ ,\ y_3=-y_5=-\ell$$

where the transformed coordinates are ξ_i, $\eta_i = \pm 1$ for the corner nodes and ξ_i, $\eta_i = 0$ for the mid-side nodes. After substituting these values of x_i, y_i, ξ_i, and η_i into Equations (2.14) and (2.13), and doing some algebra to simplify the expressions, x and y can be written as

$$x = \frac{h}{4}(1+\xi)^2$$

and (2.16)

$$y = \frac{\ell}{4}\eta(1+\xi)^2$$

The distance r from the crack tip to any point P on the radial line R, from Figure 2.5, can be written in terms of x and y as $r = \sqrt{\left(x^2 + y^2\right)}$. Substituting from Equation (2.16) we get

$$r = \frac{\ell}{4}(1+\xi)^2 \sqrt{\left[\left(\frac{h}{\ell}\right)^2 + \eta^2\right]}$$

$$(1+\xi) = \frac{\sqrt{r}}{\sqrt{\frac{\ell}{4}\sqrt{\left[\left(\frac{h}{\ell}\right)^2 + \eta^2\right]}}} \tag{2.17}$$

Since the element is isoparametric, the displacements within the element, u and v, are interpolated using the same functions $N_i(\xi,\eta)$ of Equation (2.14), and are

$$u = \sum_{i=1}^{8} N_i(\xi,\eta) u_i$$

(2.18)

$$v = \sum_{i=1}^{8} N_i(\xi,\eta) v_i$$

where (u_i, v_i) are the displacements of node i.

In order to calculate the strains in the element, which are given by

$$\begin{Bmatrix} \varepsilon_x \\ \varepsilon_y \\ \varepsilon_{xy} \end{Bmatrix} = \begin{Bmatrix} \dfrac{\partial u}{\partial x} \\ \dfrac{\partial v}{\partial y} \\ \dfrac{\partial u}{\partial y} + \dfrac{\partial v}{\partial x} \end{Bmatrix} \tag{2.19}$$

we first have to calculate the quantities $\frac{\partial u}{\partial \xi}, \frac{\partial u}{\partial \eta}, \frac{\partial v}{\partial \xi}$, and $\frac{\partial v}{\partial \eta}$ since

$$\begin{Bmatrix} \dfrac{\partial u}{\partial x} \\ \dfrac{\partial u}{\partial y} \end{Bmatrix} = [J]^{-1} \begin{Bmatrix} \dfrac{\partial u}{\partial \xi} \\ \dfrac{\partial u}{\partial \eta} \end{Bmatrix} \quad \text{and} \quad \begin{Bmatrix} \dfrac{\partial v}{\partial x} \\ \dfrac{\partial v}{\partial y} \end{Bmatrix} = [J]^{-1} \begin{Bmatrix} \dfrac{\partial v}{\partial \xi} \\ \dfrac{\partial v}{\partial \eta} \end{Bmatrix} \tag{2.20}$$

The matrix [J] is the Jacobian of the transformation from x-y coordinates to ξ-η coordinates, and is defined as

$$[J] = \begin{bmatrix} \dfrac{\partial x}{\partial \xi} & \dfrac{\partial y}{\partial \xi} \\ \dfrac{\partial x}{\partial \eta} & \dfrac{\partial y}{\partial \eta} \end{bmatrix} = \begin{bmatrix} \dfrac{h}{2}(1+\xi) & \dfrac{\ell}{2}\eta(1+\xi) \\ 0 & \dfrac{\ell}{4}(1+\xi)^2 \end{bmatrix} \tag{2.21}$$

The determinant of the Jacobian is needed in the calculation of the inverse; the determinant of the Jacobian is

$$\det|J| = \frac{h\ell}{8}(1+\xi)^3 \tag{2.22}$$

and inverting the Jacobian gives

$$[J]^{-1} = \frac{1}{\det|J|} \begin{bmatrix} \dfrac{\partial y}{\partial \eta} & -\dfrac{\partial y}{\partial \xi} \\ -\dfrac{\partial x}{\partial \eta} & \dfrac{\partial x}{\partial \xi} \end{bmatrix} = \begin{bmatrix} \dfrac{2}{h(1+\xi)} & \dfrac{-4\eta}{h(1+\xi)^2} \\ 0 & \dfrac{4}{\ell(1+\xi)^2} \end{bmatrix} \tag{2.23}$$

For simplification later, we will use the notation

$$[J]^{-1} = \begin{bmatrix} I_{11} & I_{12} \\ I_{21} & I_{22} \end{bmatrix} \tag{2.24}$$

The derivatives of u, v with respect to ξ, η are

$$\frac{\partial u}{\partial \xi} = \sum_{i=1}^{8} \frac{\partial N_i}{\partial \xi} u_i \quad , \quad \frac{\partial u}{\partial \eta} = \sum_{i=1}^{8} \frac{\partial N_i}{\partial \eta} u_i$$

$$\frac{\partial v}{\partial \xi} = \sum_{i=1}^{8} \frac{\partial N_i}{\partial \xi} v_i \quad , \quad \frac{\partial v}{\partial \eta} = \sum_{i=1}^{8} \frac{\partial N_i}{\partial \eta} v_i \tag{2.25}$$

where

$$\frac{\partial N_i}{\partial \xi} = \begin{array}{l} \frac{1}{4}\left[\xi_i(1+\eta\eta_i)+2\xi(1+\eta\eta_i)-\xi_i\left(1-\eta^2\right)\right]\xi_i^2\eta_i^2 \\ -\xi(1+\eta\eta_i)\left(1-\xi_i^2\right)\eta_i^2+\frac{1}{2}\xi_i\left(1-\eta^2\right)\left(1-\eta_i^2\right)\xi_i^2 \end{array} \tag{2.26}$$

$$\frac{\partial N_i}{\partial \eta} = \begin{array}{l} \frac{1}{4}\left[\eta_i(1+\xi\xi_i)+2\eta(1+\xi\xi_i)-\eta_i\left(1-\xi^2\right)\right]\xi_i^2\eta_i^2 \\ -\eta(1+\xi\xi_i)\left(1-\eta_i^2\right)\xi_i^2+\frac{1}{2}\eta_i\left(1-\xi^2\right)\left(1-\xi_i^2\right)\eta_i^2 \end{array} \tag{2.27}$$

Substituting the known quantities (ξ_i, η_i) at each node (i =1…8) into Equations (2.26) and (2.27), and then substituting these into Equation (2.25) yields

$$\begin{aligned} \frac{\partial u}{\partial \xi} = & \left[\frac{u_1}{4}\left(-2+3\eta-\eta^2\right)+u_2(1-\eta)+\frac{u_3}{4}\left(\eta+\eta^2\right)+\frac{u_4}{2}\left(1-\eta^2\right)\right. \\ & \left.-\frac{u_5}{4}\left(-\eta+\eta^2\right)+u_6(1+\eta)+\frac{u_7}{4}\left(-2-3\eta-\eta^2\right)-\frac{u_8}{2}\left(1-\eta^2\right)\right] \\ & +(1+\xi)\left[\frac{u_1}{2}(1-\eta)-u_2(1-\eta)+\frac{u_3}{2}(1-\eta)+\frac{u_5}{2}(1+\eta)-u_6(1+\eta)+\frac{u_7}{2}(1+\eta)\right] \end{aligned} \tag{2.28}$$

$$\begin{aligned} \frac{\partial u}{\partial \eta} = & \left[\frac{u_1}{4}(-2+4\eta)+\frac{u_7}{4}(2+4\eta)-2u_8\eta\right]^* \\ & +(1+\xi)\left[\frac{u_1}{4}(3-2\eta)-u_2+\frac{u_3}{4}(1+2\eta)-u_4\eta+\frac{u_5}{4}(-1+2\eta)+u_6-\frac{u_7}{4}(-3+2\eta)+u_8\eta\right] \\ & +(1+\xi)^2\left[-\frac{u_1}{4}+\frac{u_2}{2}-\frac{u_3}{4}-\frac{u_5}{4}-\frac{u_6}{2}-\frac{u_7}{4}\right] \end{aligned} \tag{2.29}$$

The derivatives $\frac{\partial v}{\partial \xi}, \frac{\partial v}{\partial \eta}$ are exactly the same, except every u_i in Equations (2.28) and (2.29) are replaced by the corresponding v_i.

From Equation (2.29), it is observed that the first term, denoted by *, will be equal to zero if the constraint is imposed that the displacements at nodes 1, 7, and 8 are equal,

$$u_1 = u_7 = u_8$$

and (2.30)

$$v_1 = v_7 = v_8$$

For any point along the line θ = constant (η = constant), $\frac{\partial u}{\partial \xi}, \frac{\partial u}{\partial \eta}, \frac{\partial v}{\partial \xi}$, and $\frac{\partial v}{\partial \eta}$ from Equations (2.28) and (2.29) can be written in the form

$$\begin{aligned}
\frac{\partial u}{\partial \xi} &= a_0 + a_1(1+\xi) \\
\frac{\partial u}{\partial \eta} &= b_0 + b_1(1+\xi) + b_2(1+\xi)^2 \\
\frac{\partial v}{\partial \xi} &= c_0 + c_1(1+\xi) \\
\frac{\partial v}{\partial \eta} &= d_0 + d_1(1+\xi) + d_2(1+\xi)^2
\end{aligned} \tag{2.31}$$

where a_0, a_1, b_0, b_1, b_2, c_0, c_1, d_0, d_1, d_2 are constants for any given set of nodal displacements and for any line θ = constant.

Now, calculating the strains in Equation (2.29) using Equation (2.20) yields

$$\begin{Bmatrix} \dfrac{\partial u}{\partial x} \\ \dfrac{\partial u}{\partial y} \end{Bmatrix} = \begin{bmatrix} I_{11} & I_{12} \\ I_{21} & I_{22} \end{bmatrix} \begin{Bmatrix} \dfrac{\partial u}{\partial \xi} \\ \dfrac{\partial u}{\partial \eta} \end{Bmatrix} \quad \text{and} \quad \begin{Bmatrix} \dfrac{\partial v}{\partial x} \\ \dfrac{\partial v}{\partial y} \end{Bmatrix} = \begin{bmatrix} I_{11} & I_{12} \\ I_{21} & I_{22} \end{bmatrix} \begin{Bmatrix} \dfrac{\partial v}{\partial \xi} \\ \dfrac{\partial v}{\partial \eta} \end{Bmatrix} \tag{2.32}$$

and
$$\begin{aligned} \frac{\partial u}{\partial x} &= I_{11}\frac{\partial u}{\partial \xi} + I_{12}\frac{\partial u}{\partial \eta} \\ &= \frac{2a_0}{h(1+\xi)} + \frac{2a_1}{h} - \frac{4\eta b_0}{h(1+\xi)^2} - \frac{4\eta b_1}{h(1+\xi)} - \frac{4\eta b_2}{h} \end{aligned} \tag{2.33}$$

Collecting the terms containing the different powers of (1+ξ) and substituting for (1+ξ) in terms of $\sqrt{r}$ from Equation (2.17) yields

$$\frac{\partial u}{\partial x} = \frac{A_0}{\sqrt{r}} + \frac{b_0'}{r} + A_1 \tag{2.34a}$$

where A_0, b_0', A_1 are independent of radius r and are constants for any radial line (θ = constant).

Similarly,

$$\begin{aligned} \frac{\partial u}{\partial y} &= I_{22}\frac{\partial u}{\partial \eta} \qquad (I_{21} = 0) \\ &= \frac{4b_0}{\ell(1+\xi)^2} + \frac{4b_1}{\ell(1+\xi)} + \frac{4b_2}{\ell} \end{aligned}$$

$$\frac{\partial u}{\partial y} = \frac{B_0}{\sqrt{r}} + \frac{b_0''}{r} + B_1 \tag{2.34b}$$

The derivatives of v with respect to x and y are similar and can be written as

$$\frac{\partial v}{\partial x} = \frac{C_0}{\sqrt{r}} + \frac{d_0'}{r} + C_1 \tag{2.34c}$$

$$\frac{\partial v}{\partial y} = \frac{D_0}{\sqrt{r}} + \frac{d_0''}{r} + D_1 \tag{2.34d}$$

In Equations (2.34b-d), $B_0, b''_0, B_1, C_0, d'_0, C_1, D_0, d''_0$, and D_1 are also constants independent of r.

If the constraints from Equation (2.30) are imposed, namely, that the displacements at the three crack-tip nodes are forced to be the same, then Equations (2.31) reduce to

$$\begin{aligned}
\frac{\partial u}{\partial \xi} &= a_0 + a_1(1+\xi) \\
\frac{\partial u}{\partial \eta} &= b_1(1+\xi) + b_2(1+\xi)^2 \\
\frac{\partial v}{\partial \xi} &= c_0 + c_1(1+\xi) \\
\frac{\partial v}{\partial \eta} &= d_1(1+\xi) + d_2(1+\xi)^2
\end{aligned} \qquad (2.35\text{a-d})$$

The derivatives of u, v with respect to x, y then reduce to

$$\begin{aligned}
\frac{\partial u}{\partial x} &= \frac{A_0}{\sqrt{r}} + A_1 \\
\frac{\partial u}{\partial y} &= \frac{B_0}{\sqrt{r}} + B_1 \\
\frac{\partial v}{\partial x} &= \frac{C_0}{\sqrt{r}} + C_1 \\
\frac{\partial v}{\partial y} &= \frac{D_0}{\sqrt{r}} + D_1
\end{aligned} \qquad (2.36\text{a-d})$$

As $r \to 0$, the terms in (2.34a-d) tend to $O\left(\frac{1}{r}\right)$ and the terms in (2.36a-d) tend to $O\left(\frac{1}{\sqrt{r}}\right)$.

The terms in (2.36a-d) represent the components of strain when the nodes at the crack-tip are constrained to have the same displacement, and the resulting $\frac{1}{\sqrt{r}}$ singularity is the necessary stress and strain singularity required for linear elastic fracture mechanics. The terms in (2.34a-d) represent the components of strain when the nodes at the crack-tip are initially coincident, but can then displace independently, and the $\frac{1}{r}$ singularity that is obtained is characteristic of perfect plasticity, and blunting of the crack-tip is obtained during loading.

CHAPTER 3

MODELING ON $MoSi_2$/Nb COMPOSITES USING THE HYBRID ELEMENT METHOD

3.1 Experimental Procedure

$MoSi_2$ composites reinforced with 20 vol. % of Nb layers and 20 vol. % zirconia particles stabilized with 2 mole % yttria (TZ-2Y) were fabricated by the Material Science Department of The Ohio State University. The Nb foils were made with a thickness of ~ 200 μm. The microstructures of the composites are shown in Figures 3.1(a) and 3.1(b). The Nb layers and a layered interfacial structure (consisting of (Mo, Nb)$_5$Si$_3$ and a Nb_5Si_3 layer) are also evident in the above figures. The material properties of the composites are listed in Table 3.1.

Property	$MoSi_2$	Nb	Nb_5Si_3
Elastic modulus, E (GPa)	380	103	300
Poisson's ratio,	0.17	0.38	0.17

Table 3.1 Constituent Property Data [ASM Metals Handbook, 1990]

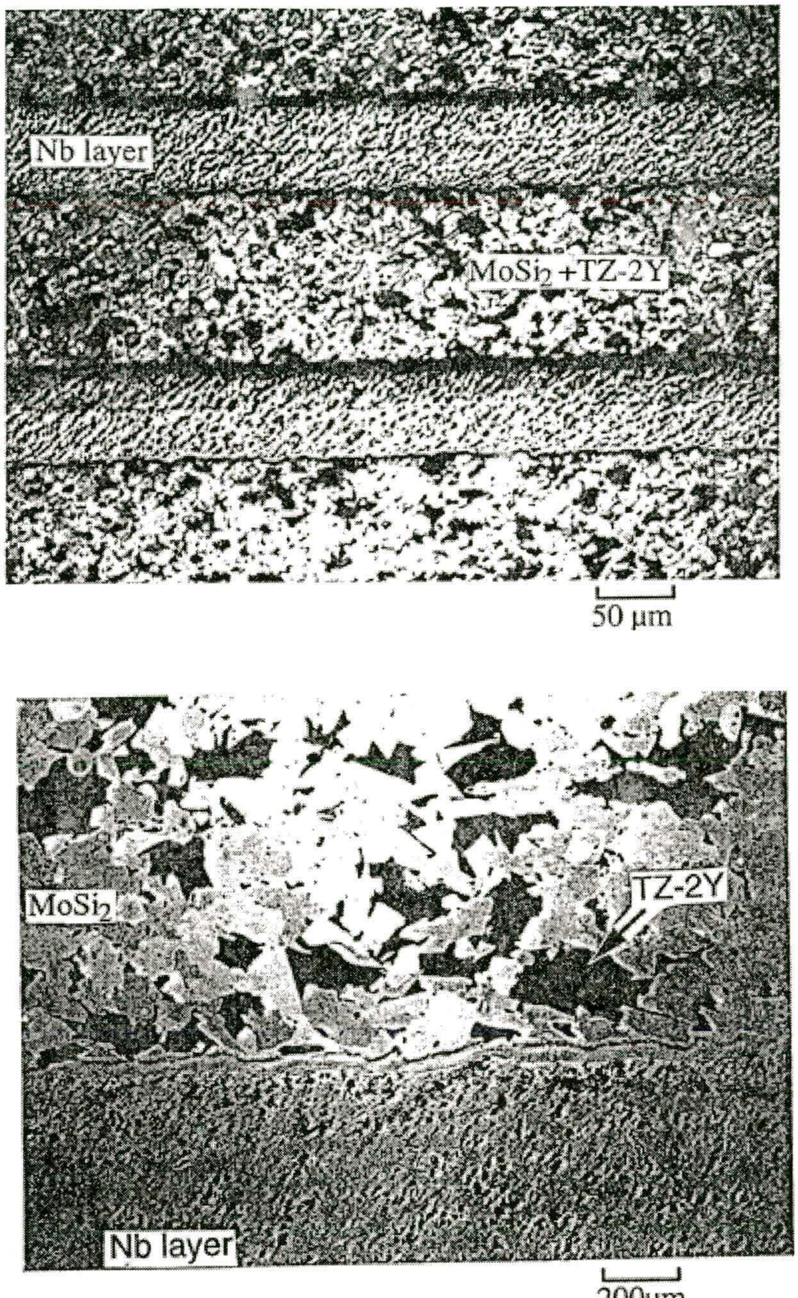

Figure 3.1(a), (b) Microstructure of $MoSi_2$ composite reinforced with 20 Vol.% TZ-2Y and 20 Vol.% Nb Laminate

3.1.1 Fracture Toughness

Fracture toughness tests were performed by Fan Ye of the Material Science Department of The Ohio State University on Single Edge Notched (SEN) bend test samples with relatively deep notches (notch-to-width ratios of 0.4). The SEN specimens were produced by electro-discharge machining (EDM) techniques. The fracture toughness tests were performed in accordance with the ASTM E399 code [ASTM, 1948]. The specimens were initially pre-cracked under far-field compression loading [Brockenbrough and Suresh, 1988]. Precracking was used at a stress ratio Kmin/Kmax of 0.1 to produce an atomistically 'sharp' crack-tip. This was required to ensure that sufficiently high crack-tip triaxiality levels were maintained during the tests. Fracture toughness tests were then carried out under three-point loading at a loading rate corresponding to a stress intensity factor increase rate of 0.92 $\mathrm{MPa}\sqrt{m}\cdot s^{-1}$. The failure modes in the fractured specimens were then examined using scanning electron microscopy (SEM) techniques.

3.1.2 Resistance Curve (R-Curve) Behavior

R-curve tests were performed on Single Edge Notched (SEN) bend test samples by Fan Ye. The specimens were initially pre-cracked under far-field compression loading [Brockenbrough and Suresh, 1988] to produce a sharp pre-crack. A load corresponding to the lower stress intensity factor (below the initiation toughness) was applied and quickly removed. The specimen was then examined under an optical microscope. The applied loads were increased in increments of 5 % if no crack growth was detected.

3.2 Numerical Simulation

3.2.1 Main Crack Problem

In this study the finite element method is used to analyze the effect of layers and interfaces on the crack propagation phenomena in three point bending experiments, as shown in Figure 3.2. The concentrated load P is specified to be 1647.89N to simulate a typical fracture toughness testing condition. The special crack tip element developed by Zhang [Zhang, 1995] based on the hybrid method was used to directly evaluate stress intensity factors at the crack tip. One 17 node linear crack tip element and approximately 2000 4 node linear elements were used in the analysis. In this numerical analysis, the material properties of matrix, layers, and interfaces were also assumed to be linearly elastic and isotropic. The mechanical properties are summarized in Table 3.1. The interfacial region in the first layer ahead of the crack tip (the fourth layer counting from the bottom of the beam in Figure 3.2) was included in this analysis, while the interfacial regions for other layers were ignored. Since the interfacial region is very thin, the above approximation was sufficient to model the effect of interfacial regions on the behavior of the major crack tip.

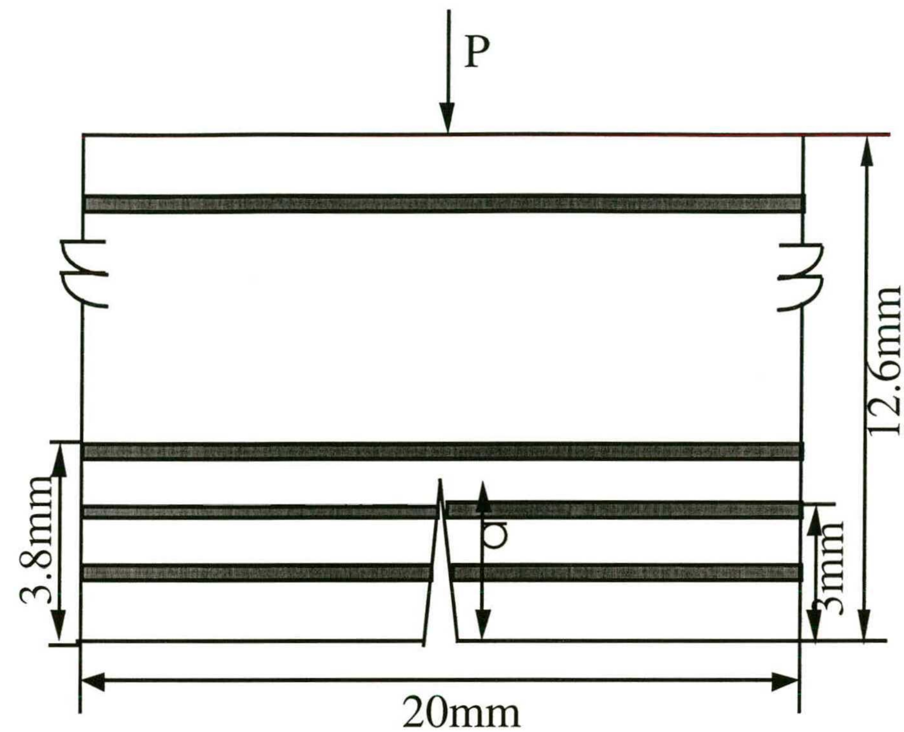

Fig. 3.2 Three point bending simulation

The deformation is predominantly mode I, and, therefore, the stress intensity factor, K_I, is plotted as a function of the crack length, a, as in Figure 3.3. The results obtained for the composite are compared to those obtained for a monolithic sample consisting solely of the matrix material. In both the composite and monolithic cases, the longer the crack length, the larger the K_I value becomes. For crack lengths between 3.1mm and 3.78 mm, the K_I values of the composite are slightly larger than those of the monolithic alloy. When the crack tip in the composite is far away from the layer, the crack tip behavior is basically determined by the overall material properties of the sample. Since the overall elastic moduli of the composite are smaller than those of the monolithic alloy, the small increase in the stress intensity factors is attributed mainly to the lower moduli of the Nb reinforcement. When the crack length is 3.79 mm, since the layer is located 0.01 mm ahead of the crack tip, a significant increase in the K_I value in the composite is observed. In contrast, in the case of monolithic $MoSi_2$, very little change is observed. It is evident that, as the main crack approaches the layer, the crack is locally attracted to the softer layer. This is consistent with the results of previous analyses by Budiansky [Budiansky, 1986].

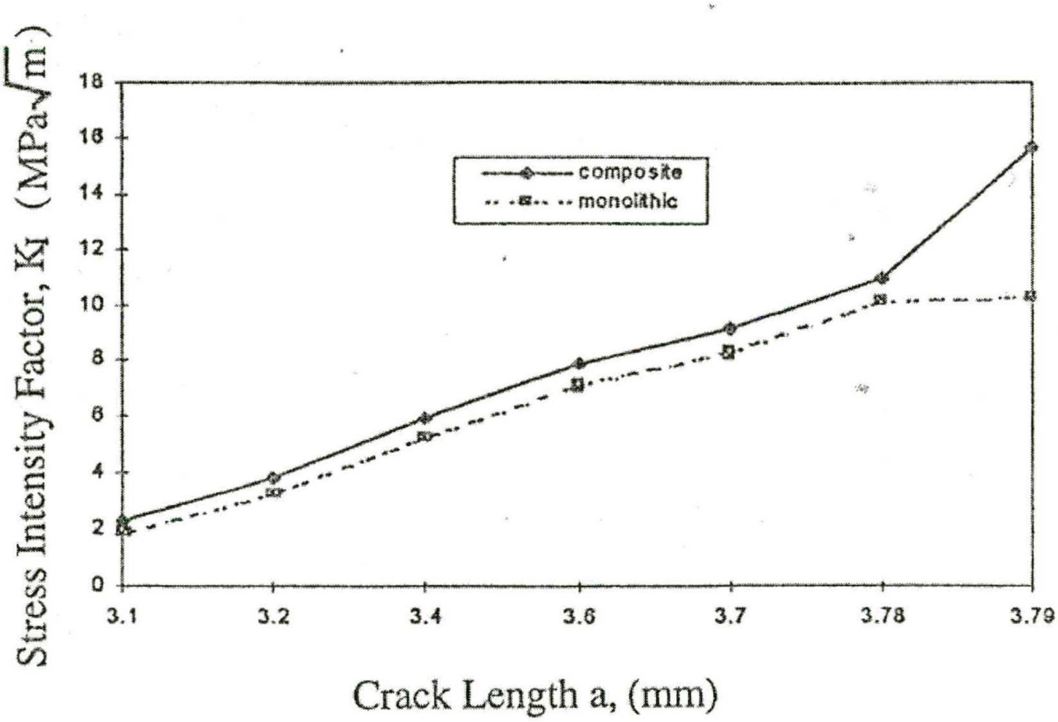

Figure 3.3 K_I Versus Main Crack Length

3.2.2 Debonding Crack Problem

Since debonding was observed in the composites prior to the onset of the crack bridging (Figure 3.4), the debonding crack problem shown schematically in Figure 3.5 was analyzed. Only a portion of the three-point bending experiment was considered in the analysis: the portion was cut from the whole specimen in the numerical analysis. The outer boundary stress distribution of this portion is imported from the corresponding main crack problem we previously analyzed. Since the region under consideration is sufficiently large, it is assumed that the inclusion of the debonding cracks will not significantly change the stress distribution on the outer boundary. The debonding is assumed to occur in the interfacial region, and is symmetric relative to the main crack. Two 17 node linear crack tip elements and approximately 2500 4 nodes linear elements were used once again.

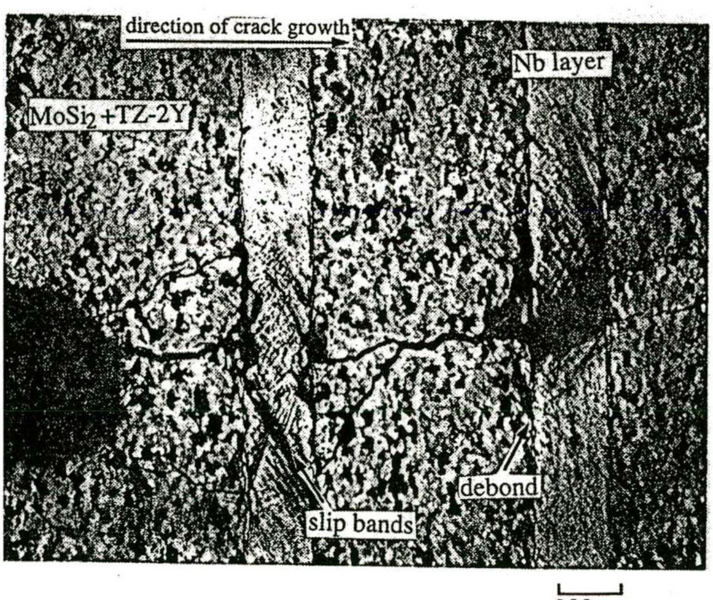

Figure 3.4 Interaction of crack and microstructure (crack bridging and blunting) in SEN fracture specimen before final fracture

Figure 3.4 Interaction of crack and microstructure (crack bridging and blunting) in SEN fracture specimen before final fracture

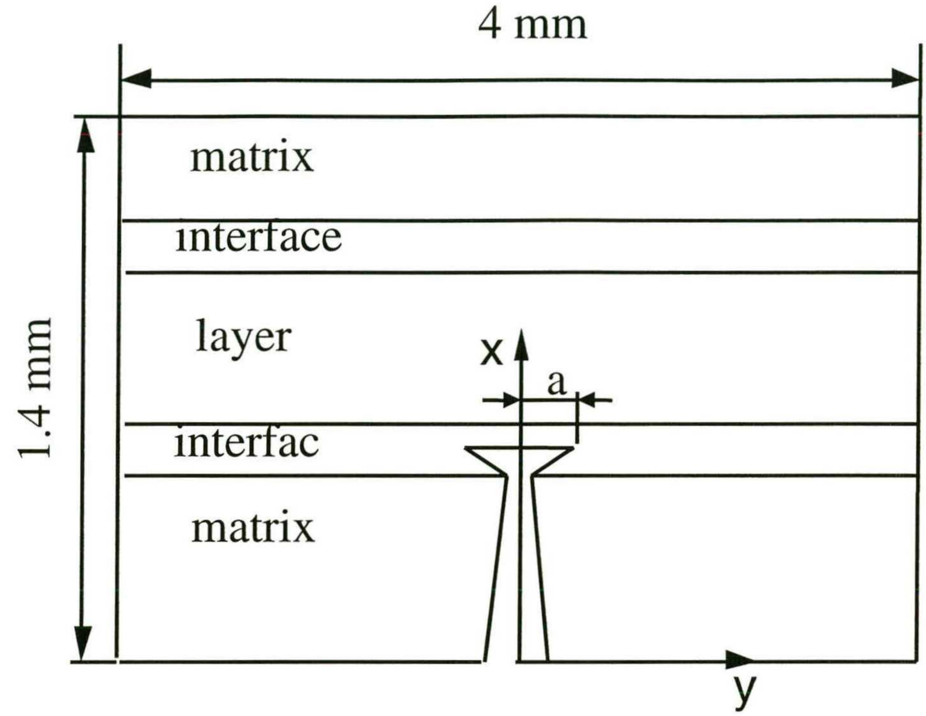

Fig.3.5 Debonding Crack Problem

The stress intensity factors, K_I and K_{II}, and the mixity ratio, K_I/K_{II}, at the debonding crack tips are plotted as a function of the crack length, d, in Figure 3.6. For long debond lengths, the values of K_I and K_{II} increase slightly, and the mode mixity ratio, K_I/K_{II}, decreases. Also, when the extent of debonding is small, the driving force for debonding remains almost constant with increased debond length. The mode mixity also remains almost constant.

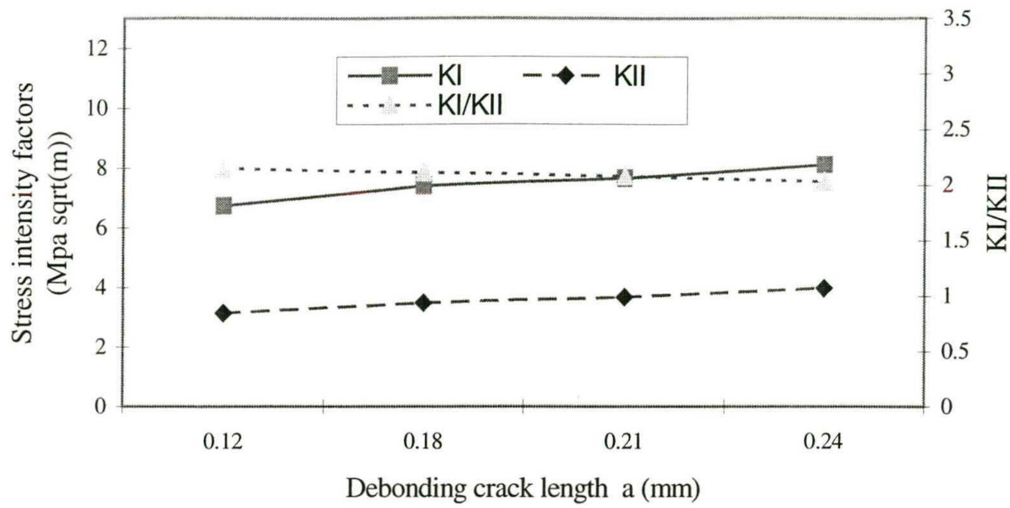

Fig 3.6 Stress Intensity Factors versus Debonding Length

Finally, in Figure 3.7, for a= 0.12 mm and a=0.24mm, the maximum normal and shear strains are plotted as a function of the distance from the debonding crack tip in the x direction. In both cases, the strains are apparently beyond the elastic limit in the vicinity of the debonding crack tips. However, approximately 0.3 mm away from the debonding crack tips, the strains become sufficiently small to be considered elastic. This result shows that the plastic region is limited to the region immediately ahead of the debonding crack tips. At the interfacial region, the strains reach local maximum, and the direction of the maximum strain is almost in the y direction. In general, the strains at a=0.24 mm are larger than those at a =0.12 mm. When a=0.24mm, the value of the maximum shear strain reaches 0.25 % at the interface. Hence, debonding is likely to occur at the other interface, assuming that the plastic region around the debonding crack tips will not significantly influence the stress distribution away from the crack tips. Since the critical strain states are reached at two points symmetric to the major crack, debonding at the other interface is likely to occur spontaneously and symmetrically. Once the debonding occurs at the other interface, the plastic regions around the new debonding crack tips will influence the plastic regions around the original debonding crack tips. Further plastic deformation within the Nb layer will dominate behavior beyond this point.

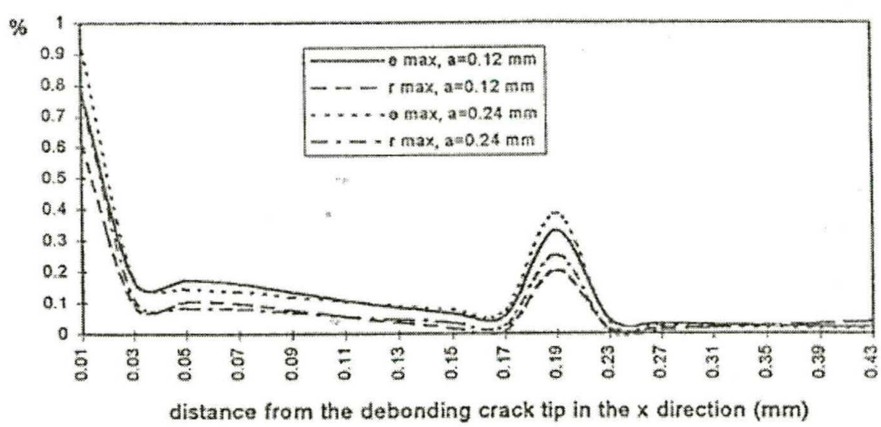

Fig.3.7 Maximum Normal and Shear Strains

3.3 CONCLUSION

Crack/microstructure interactions have been studied in a layered $MoSi_2$/Nb composite. The studies reveal that the crack/microstructure interactions give rise to shielding due to crack-tip blunting and crack bridging. Under the assumption that the material is monolithic, i.e., pure $MoSi_2$, the finite element analysis gave the same K_I as the results from the hand book solution [ASTM, 1981]. This proves that our finite element analysis is correct. Finally the numerical result of $K_I = 16.6$ MPa$\sqrt{m}$ gave the true K_I of the $MoSi_2$/Nb composites.

Finite element models of the observed crack/microstructure interactions were also developed. The models show that the matrix cracks in the $MoSi_2$ are attracted to the softer Nb layers, especially when the cracks are very close to the Nb layers. The driving force for debonding and the mode mixity were found to remain constant with increased debond length.

CHAPTER 4

MODELING ON NiAl/V COMPOSITES USING THE FINITE ELEMENT METHOD

4.1 Introduction and Experimental Procedure

There has been considerable interest in NiAl as a candidate material for intermediate-temperature applications in aerospace vehicles [Miracle, 1993 , Noebe et al., 1991]. This interest has been due largely to its attractive combinations of excellent oxidation resistance (up to 1300 - 1400 ^{0}C), moderate density (5.90 gcm^{-3}) and intermediate strength retention (up to 600 ^{0}C) [Miracle, 1993 , Noebe et al., 1991]. Unfortunately, however, the possible structural applications of NiAl have been limited by its low room-temperature fracture toughness (~5 - 7 MPa$\sqrt{m}$) [Miracle, 1993 , Noebe et al., 1991]. This has stimulated extensive efforts aimed at toughening NiAl via intrinsic [Bowman et al., 1992, George and Liu, 1990] and extrinsic [Chen et al., 1995, Heredia et al., 1993, Joslin et al., 1995, Noebe et al., 1991, Ramasundaram et al., 1998, Subramanian et al., 1994] modification.

Intrinsic modification of NiAl via alloying has not resulted in significant toughening [Bowman et al., 1992, George and Liu, 1990]. In contrast, extrinsic toughening via ductile phase reinforcement (composite approach) has been shown to promote significant improvements in the fracture toughness of NiAl. Ductile phase reinforcement with refractory metal particles and fibers has been shown to significantly improve the fracture toughness of NiAl to levels between ~11 - ~ 30 MPa$\sqrt{m}$ [Chen et al., 1995, Heredia et al., 1993, Joslin et al., 1995, Noebe et al., 1991, Ramasundaram et al., 1998, Subramanian et al., 1994).

The possible use of vanadium microlaminates in the toughening of NiAl composites is examined here. Ductile layer reinforcement has been shown to offer higher toughening of brittle intermetallics than ductile particles and fibers. Vanadium layers with thicknesses of 100, 200 and 400 μm are shown to significantly improve the fracture toughness of NiAl. The extent of toughening, which increases with increasing layer thickness, is attributed to crack bridging and the interactions of propagating cracks with vanadium layers. Finite element models are used to explain the re-initiation of cracks in adjacent NiAl layers after retardation by the vanadium layers in the crack arrestor orientation.

NiAl/V composites reinforced with 20 vol. % of vanadium layers were fabricated by Mingwei Li of the Material Science Department of The Ohio State University. The vanadium layers have thicknesses of 100, 200 and 400 μm. The microstructures of the composites are shown in Figures 4.1(a-d). A small interfacial layer was also observed to form between the NiAl and vanadium layers (Figure 4.1 d).

The initiation fracture toughness and the resistance-curve behavior test of the NiAl/V microlaminates were studied using 38.1 mm long single edge notched (SEN) specimens with rectangular cross sections (15.24 mm x 6.35 mm), and the experimental test was done by Mingwei Li. The SEN specimens were pre-cracked in cyclic compression prior to fracture experiments under three-point bending. The specimens were loaded in incremental stages until crack initiation from the pre-cracks was observed. The loads were then increased in 5% increments to promote stable crack growth until specimen fracture occurred. The crack/microstructure interactions associated with stable crack growth were monitored with an optical microscope before each load increment. The fracture toughness of monolithic NiAl was measured using SEN specimens of the same dimensions to obtain the matrix toughness value. Tensile tests were also performed on thin vanadium thin foils and single layer composite systems in an effort to determine the constitutive laws for the different layer thicknesses.

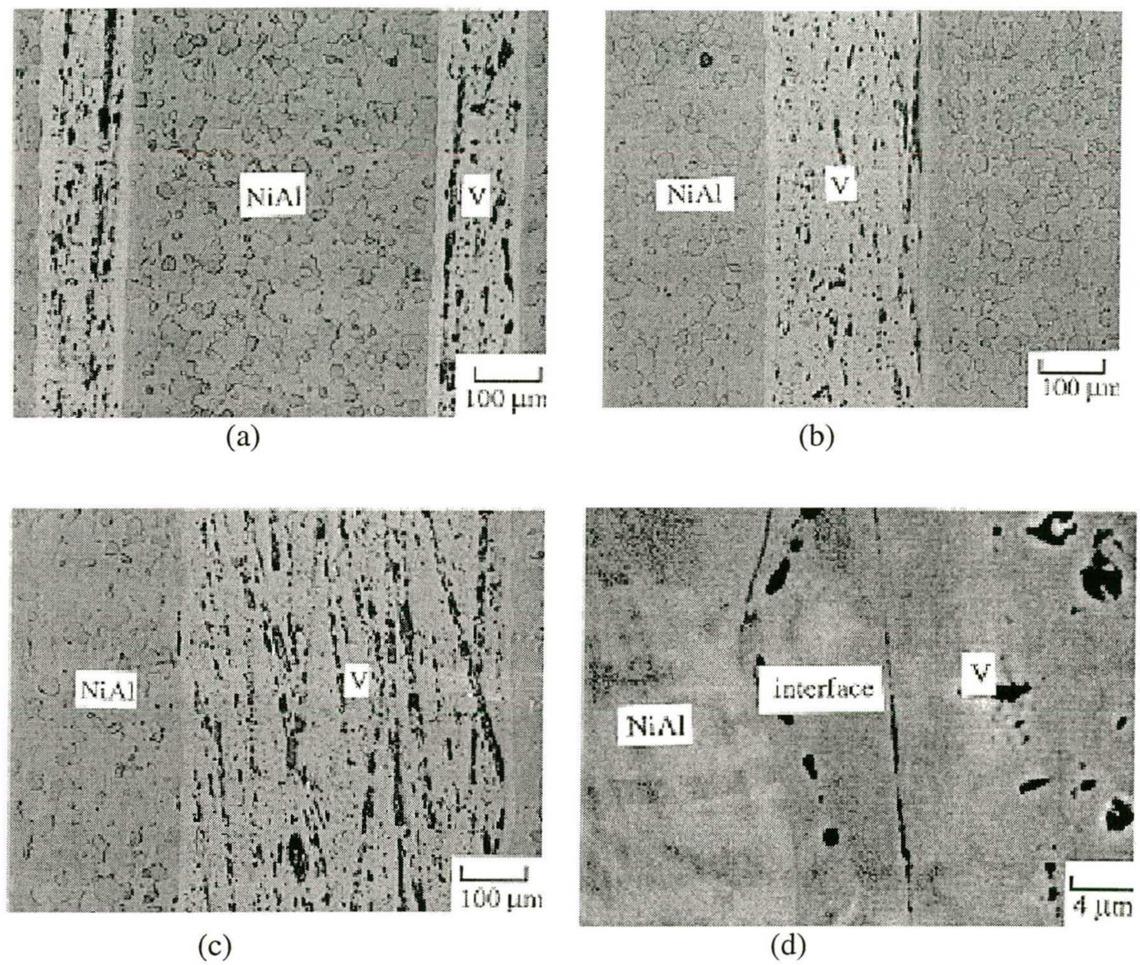

Figure 4.1 (a)~(d) Typical microstructure of NiAl/V composites: Optical micrograph of NiAl composites reinforced with (a) 100 μm thick vanadium layer, (b) 200 μm thick vanadium layer, and (c) 400 μm thick vanadium layer, and (d) SEM micrograph of the interface between NiAl and vanadium layers.

4.2 Finite Element Modeling with ABAQUS

Finite element simulation of three point bending experiments of the NiAl/V composites as in Figure 4.2 (ASTM E-399 tests) [M. Li and R. Wang 1998] were conducted. The plastic deformation in vanadium is evident as seen in Figure 4.11 ~ Figure 4.13. Therefore, instead of using the hybrid method developed by J. Zhang [J.Zhang, 1995], which can only handle linear elastic material, the local strain distributions and J integrals around the crack tip associated with the microstructure configurations are modeled using the finite element package ABAQUS version 5.5.

The composite is made of NiAl matrix and 20 % volume fraction of vanadium layers, and specimens with three distinct vanadium layer thicknesses (100, 200 and 400 μm) are analyzed. The height and length of the specimens are 15.28 mm and 25.4 mm. While the thickness of the specimens is 6.25 mm, the plane strain assumption is employed in all of the numerical calculations. The size of the specimens are the same, and there are 24, 13, and 6 vanadium layers, respectively, for 100, 200, and 400 μm thickness layer specimens. The initial crack length is 5.9 mm. The material properties of the NiAl and interfaces are assumed to be linearly isotropic, and the vanadium layers are assumed to be elastic-perfectly plastic with von Mises yield criteria as in Table 4.1.

Approximately 90,000 eight node iso-parametric plain strain elements are used to globally model the individual NiAl matrix, vanadium layers, and interfacial regions in order to capture the microstructure of the composites as shown in Figure 4.3, using the SDR IDEAS-4.2 software package. At the crack tips, special collapsed crack tip elements are used to capture the singularity of the crack tip associated with the elastic-perfectly plastic material behavior of the vanadium layer, as discussed in Chapter 2.

	NiAl	Vanadium	Interface
E (Gpa)	188	102.6	145
ν	0.31	0.36	0.36
Yield stress (Gpa)	---	0.4469	---

Table 4.1. Material properties of NiAl, vanadium and interface

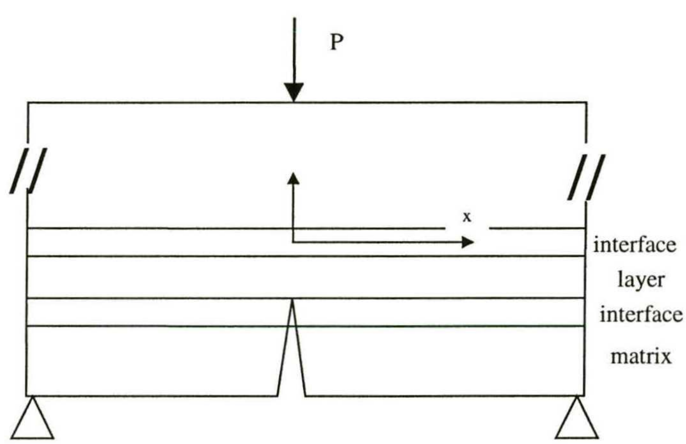

Figure 4.2. Three point bending specimen

Boundary
Condition

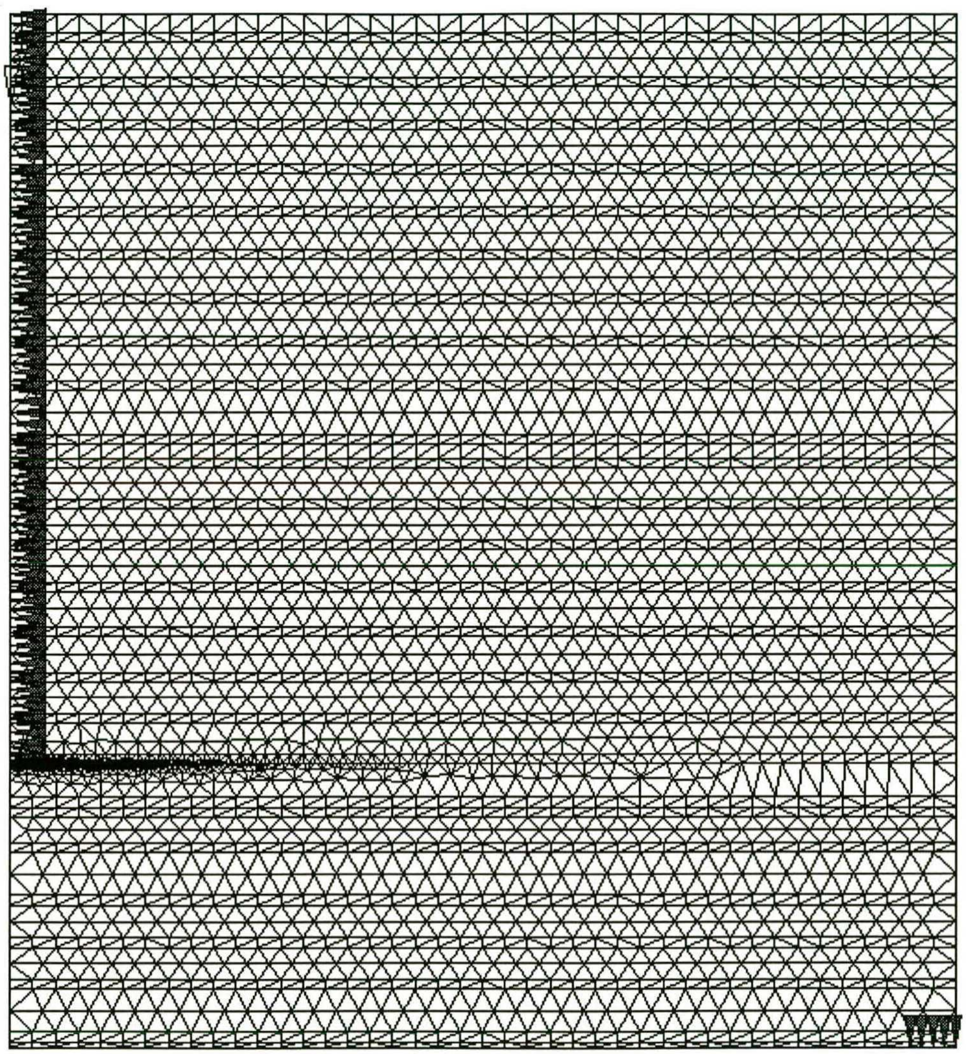

Figure 4.3 (a) FEM global mesh for 200 μm specimen
(b) FEM submodel mesh for 200μm specimen

To be continued

continued

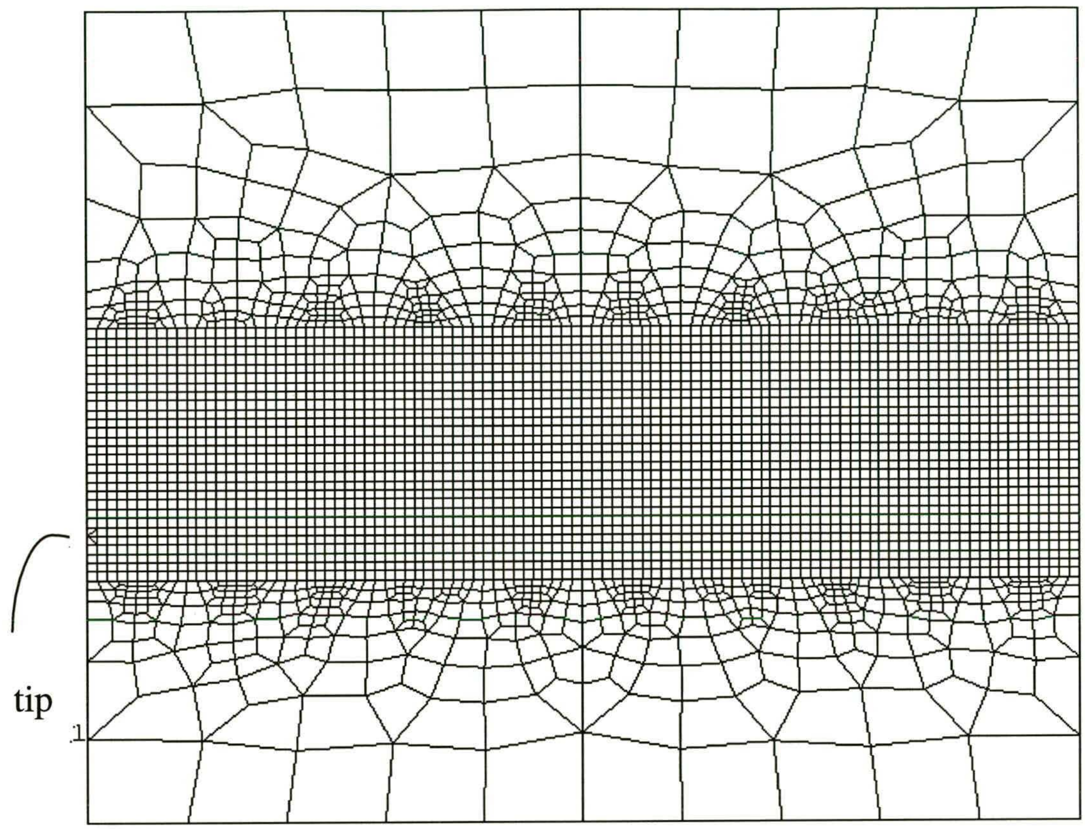

4.2.1 Submodeling

To capture the singularity at the crack tip and deal with the thin interfacial layer between NiAl and vanadium, submodeling technique is used after global modeling. Submodeling is a technique used to analyze a local part of a model with a refined mesh. It is very useful if it is important to obtain an accurate solution in the local region while the refined modeling of this region has negligible effect on the overall model. This technique works as follows. First, the overall model is meshed with relatively coarse meshes. However, the mesh must be fine enough to get accurate results for the overall problem. Then a neighboring region of the local part of interest is modeled with refined meshes. Figure 4.4 shows the submodeling of a fracture problem. In this figure, the whole domain is meshed with larger elements. The sub-region near the crack tip is meshed with very fine rosette elements as shown in figure 4.4(b). The solution of the entire model serves as the boundary of the submodel.

The boundary of the submodel is decided by interpolating the solution of the global model onto the appropriate submodel boundary nodes and by applying the prescribed boundary to this part. If the global model defines an accurate boundary for the submodel, this technique can improve the accuracy of the solution for the local region and the calculation efficiency. A general criterion for choosing the region of the local model is that the solution at the boundary of the submodel is not changed significantly by different local modeling. This requires that the submodel boundary be far enough away from the area where the solution is changed by different modeling. St. Venant's principle can be used to determine the region of the submodel approximately. In our modeling, a finer mesh at the crack tip was used through the submodel technique, and the mesh for 200 μm is shown by Figure 4.3(b).

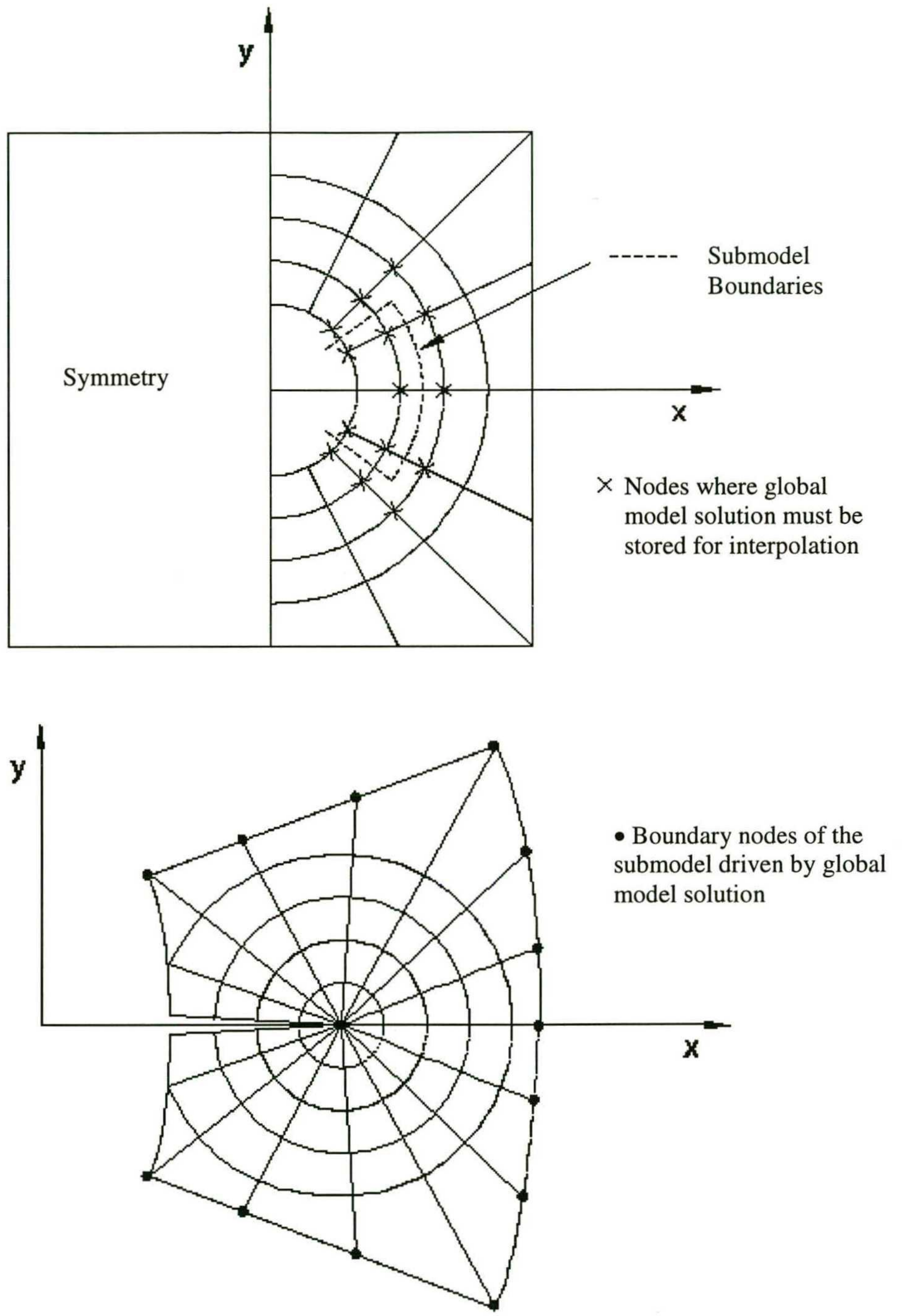

Figure 4.4 (a): Global mesh used to analyze fracture problem. (b): Submodel of the global model shown in figure 4.4 (a) [ABAQUS user's manual].

4.2.2 Plastic deformation and crack tip strain states

The vanadium had significant plastic deformation during the experiment, which means it underwent such non-recoverable deformation in a ductile fashion. The plasticity models we use in ABAQUS are "incremental" theories in which the mechanical strain rate is decomposed into an elastic part and a plastic (inelastic) part. From the tension test by Mingwei Li on vanadium (Figure 4.5), we can see that the plastic character of vanadium is almost perfect plasticity. This means the yield stress does not change with plastic strain.

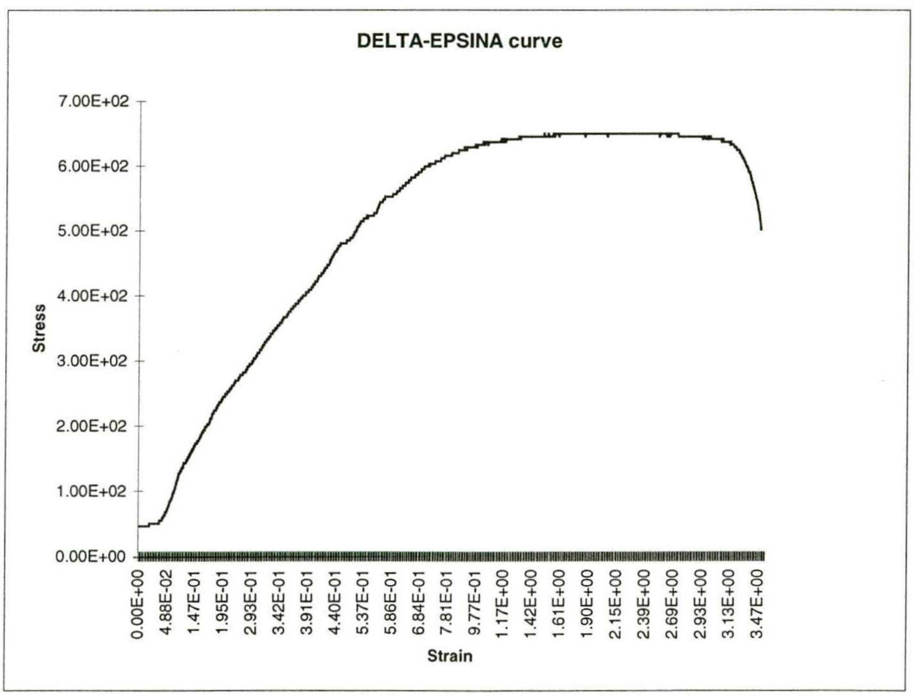

Figure 4.5 Uniaxial tension test of vanadium

In actual experiments by Mingwei Li, the load was increased with a small increments and the crack tip position is checked at each load increment. Experimentally, the crack propagation was observed to be hindered at the ductile vanadium layers and reinitiated at the other side of the layers. Whenever the crack propagation is observed to occur from one layer to the next layer, the load is recorded as the critical load for the originating layer.

From the uni-axial tension test of pure NiAl (see Figure 4.14) made by Mingwei Li of the Material Science Department of The Ohio State University, we observed that the specimen failed when the normal strain come to 0.5%. That is the critical strain of NiAl; therefore, the critical normal strain for NiAl is 0.5%, and the critical shear strain is 0.25% since in many brittle materials the critical shear strain is half the critical normal strain.

Based on the experimental observations of the re-initiation of a crack at the other interfacial region of the layers, the strain distributions of the interface layer are plotted as a function of the x axis for each incremental load as in Figure 4.7. In all the cases with three thickness layers, the critical strain states (0.25 % shear strains or 0.5% normal strains from the experiment) are observed to occur in shear strains rather than normal strains. As shown in Figure 4.7, cracks are numerically predicted to reinitiate approximately 45 degrees measured from the direction of original crack propagation. Furthermore, the direction of crack propagation is approximately 135 degrees measured from the x-axis.

It must be pointed out that observed from the experimental results of Figure 4.12 by Mingwei Li, the crack propagation path is not exactly 45 degrees at the interface. The differences are caused because in our finite element analysis, we have made the idealized assumption that the crack paths originally are vertical to the vanadium layer, but actually the crack path in the matrix is tilted.

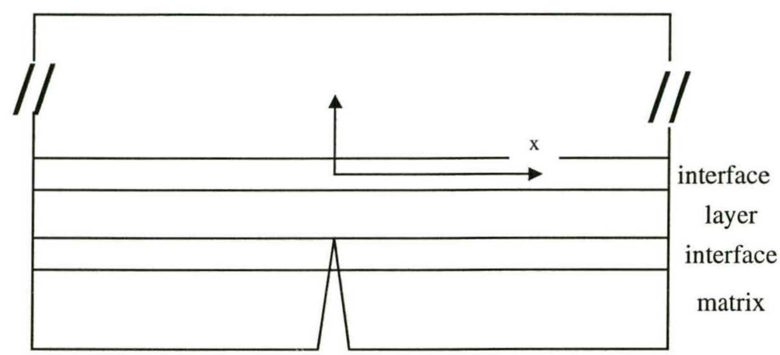

Figure 4.6 Specimen geometry and coordinate system

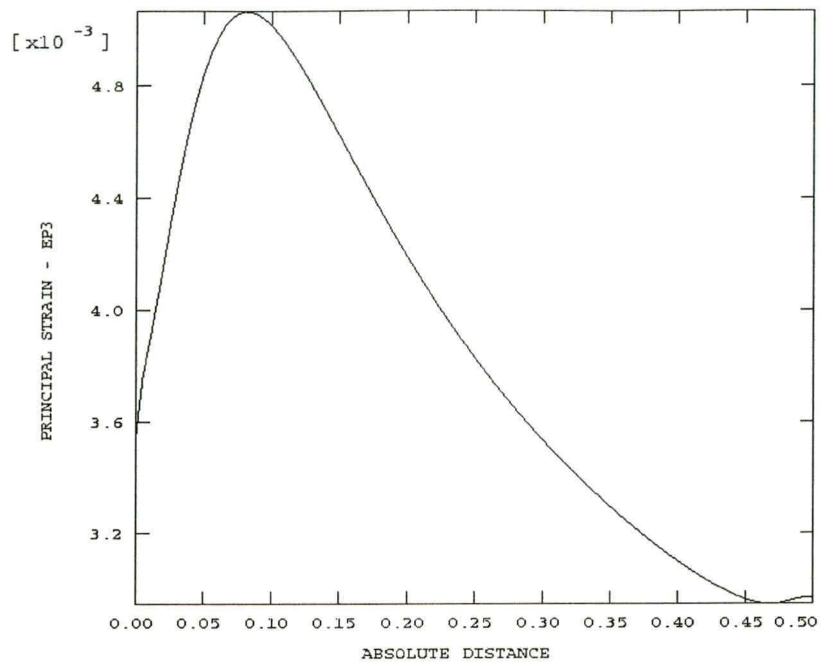

Figure 4.7(a). Maximum Principal Strain Along 100 μm Layered Structure

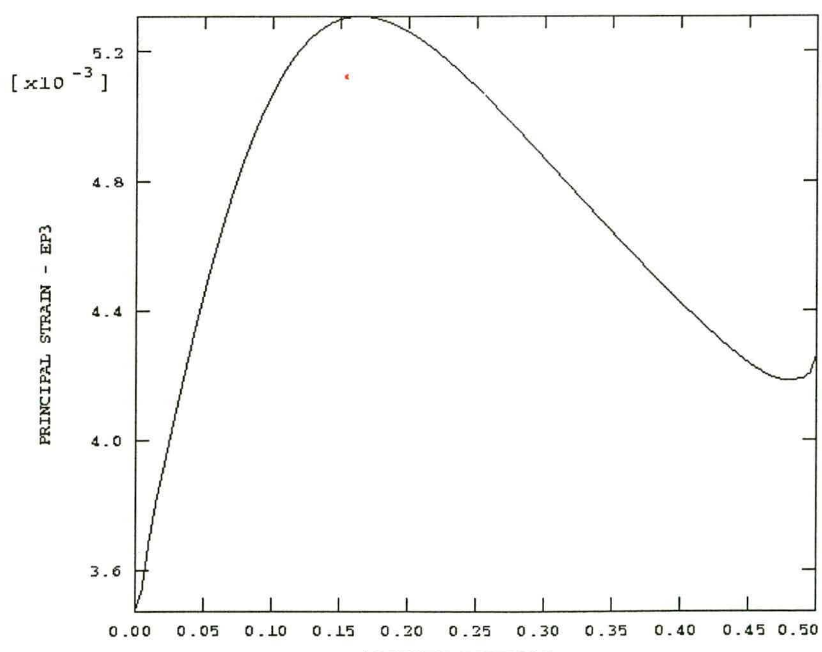

Figure 4.7(b). Maximum Principal Strain Along 200 μm Layered Structure

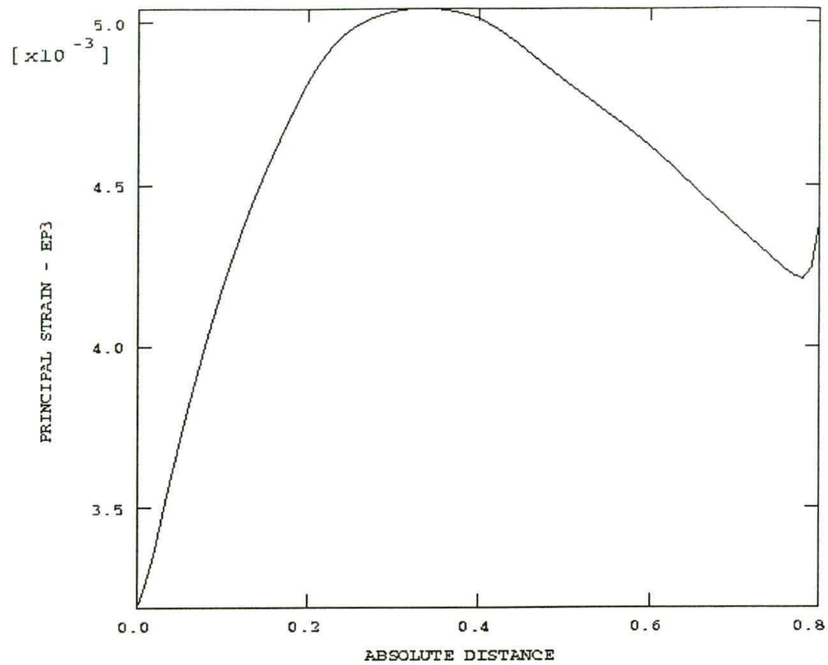

Figure 4.7(c). Maximum Principal Strain Along 400 μm Layered Structure

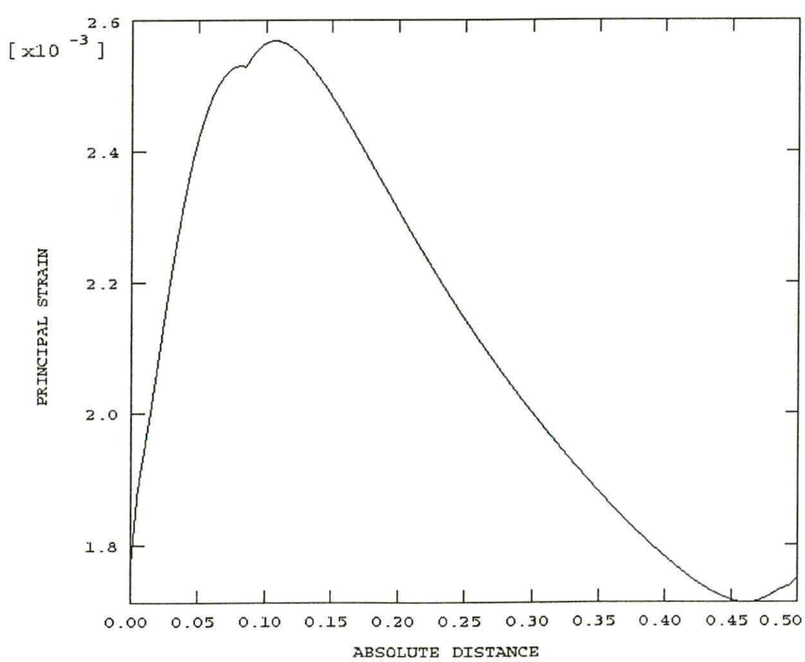

Figure 4.8(a). Maximum Shear Strain Along 100 μm Layered Structure

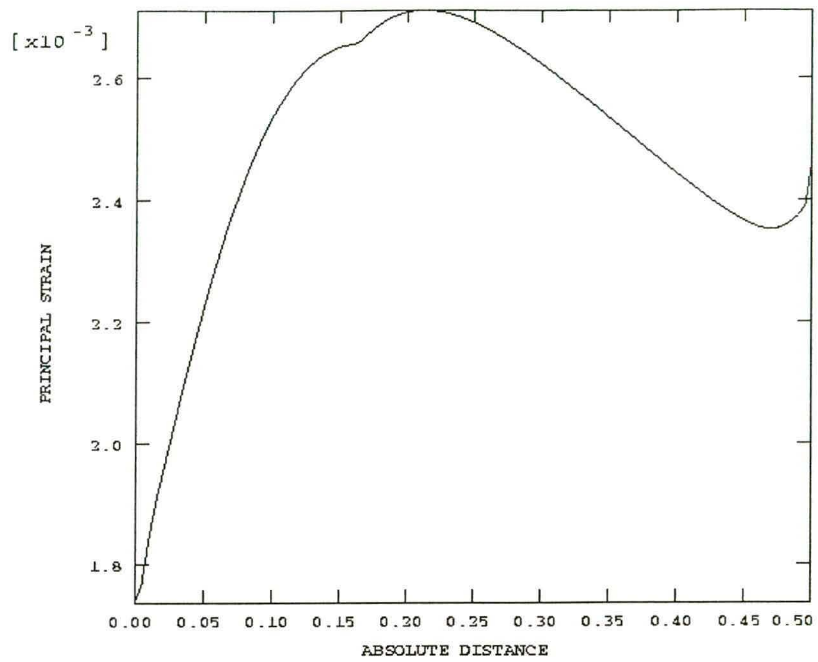

Figure 4.8(b). Maximum Shear Strain Along 200 μm Layered Structure

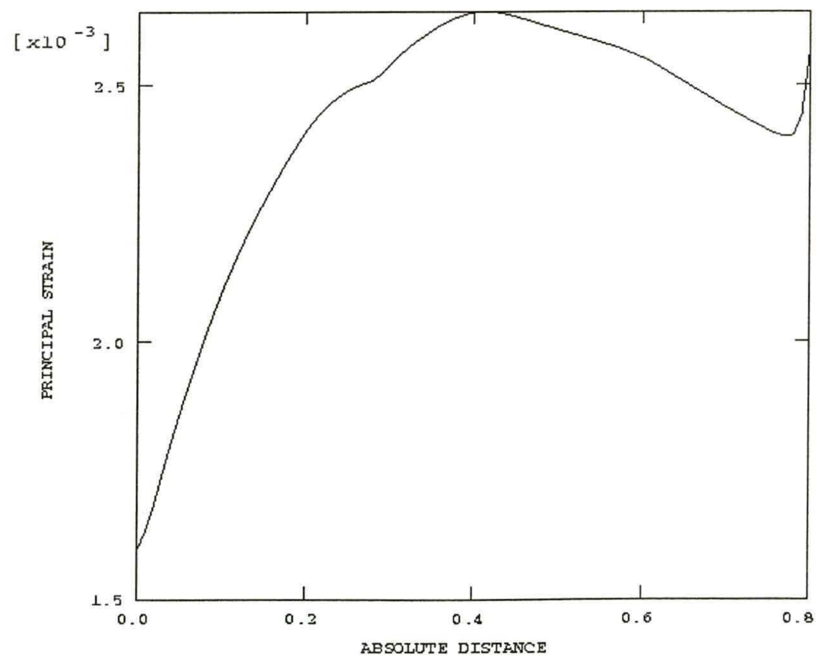

Figure 4.8(c). Maximum Shear Strain Along 400 μm Layered Structure

4.2.3 J – integral and R-curve simulations

ABAQUS offers the evaluation the J-integral for fracture mechanics studies. The J-integral is widely accepted as a fracture mechanics parameter for linear material response, as discussed in Chapter 2. For linear material response, *J* can be related to the stress intensity factor.

The J-integral is defined in terms of the energy release rate associated with crack advance. For a virtual crack advance $\lambda(s)$ in the plane of a three-dimensional fracture, the energy release rate is given by:

$$J = \int_L J(s)\lambda(s)ds = \lim_{\Gamma \to 0} \int_{S_t} \lambda(s)\mathbf{n} \cdot \mathbf{H} \cdot \mathbf{q} dS$$

where J(s) is the local value of the J-integral at a position along the crack front; the limit *L* indicates that the integration goes from one end of the crack to the other, $dS = ds\, d\Gamma$ being a surface increment along a vanishingly small tubular surface S_t enclosing the crack tip; **n** is the outward normal to S_t; and **q** is the local direction of crack propagation. **H** is given by:

$$\mathbf{H} = (W\mathbf{I} - \sigma \cdot \frac{\partial \mathbf{u}}{\partial \mathbf{x}})$$

where *W* is the strain energy density,

$$W = \int_0^{\varepsilon} \sigma \cdot d\varepsilon$$

For elastic-plastic or viscoplastic material behavior, *W* is defined as the actual strain energy density plus the plastic dissipation, thus representing the strain energy in an "equivalent elastic material."

With the divergence theorem, the contour integral can be expanded into an area integral in two dimensions, or a volume integral in three dimensions, over a finite domain surrounding the crack front. This domain integral method is used to evaluate contour integrals in ABAQUS. The method is quite robust in the sense that accurate contour integral estimates are usually obtained even with quite coarse meshes. This is because the integral is taken over a domain of elements surrounding the crack front, so that errors in local solution parameters have a lesser effect on the value calculated. Contour integrals along several different crack tips are evaluated at any time.

The loads required to achieve the critical strain states in the interfacial layers are recorded as critical loads for the layer based on the numerical simulations, and the crack is assumed to propagate in the matrix to the next vanadium layer. Experimentally, the crack propagation is no longer symmetric since a crack is observed to reinitiate at only one of the numerically predicted crack re-initiation sites. However, the crack bridging due to ductile layers is experimentally observed to be more or less symmetrical. Therefore, in the numerical simulations, cracks are assumed to reinitiate along the direction of original crack propagation. In reality, a thin interfacial layer of 15 ~ 20 μm is observed to form between the NiAl and vanadium layers. The effect of these interfacial layers on the numerical results, however, is found to be very small, and thus the interfacial layers are ignored in the subsequent numerical predictions of critical loads and J integrals. These numerical simulations are performed for three samples with three distinct thickness layers, and compared against experimental results as in Table 4.2. Despite some idealizations, numerical predictions match experimental measurements. At the critical load for each layer, J integrals are evaluated and plotted as a function of crack length increment as in Figure 4.9. When J integrals are evaluated at critical loads, the strain distributions around the crack tip show that the plastic region at the crack tip is very small and small scale yielding conditions are satisfied. Assuming that the mode I dominates the crack opening, the stress intensity factors are evaluated based on plane strain linear elastic fracture mechanics. The mode I stress intensity factors vs. crack length increments are plotted in Figure 4.10.

Finally the Resistance-curves obtained from the finite element method are compared with the handbook solutions, large scale bridging model and steady-state toughness extracted from the weight function method (Kss) as done by Mingwei Li in Figure 4.15. In the handbook solution, we assume that the material is monolithic and use the formula from the handbook [Teda et al., 1985] to calculate K_I. Under the assumptions that the bridge length is large relative to the specimen dimension and crack length, and that the overall shielding effect to the crack is the traction acting on the crack with a factor of weight function and a volume factor, [Ye and Soboyejo, 1998], [Bloer et al., 1998], the large scale bridging model gives:

$$\Delta K_{lsb} = \int_L v_f \alpha \sigma(x) h(a,x) dx$$

where L is the length of bridge zone, v_f is the volume factor, α is the constraint/triaxiality factor, $\sigma(x)$ is a traction function along the bridge zone and assumed as a constant equal to the yield stress of the monolithic vanadium layer, a is crack length, h(a, x) is a weight function given by [Fett and Munz, 1994]. Then

$K_{Isb} = K_i + \Delta K_{Isb}$

where K_i is the stress intensity factor required for re-initiation from the first layer that intercepts the propagating crack.

Assuming the specimen width is significantly greater than that of the length of the bridging zone, we can change the large scale bridging model to the small-scale bridging. Putting the small bridging condition, in which the width of the specimen goes to infinity, into the above equation, the weight function method solution (Kss) can be obtained.[Li et al., 1998]. The finite element method and Kss method provide a steady state of K_I compared with other methods, i.e., higher intrinsic small-scale bridging fracture toughness levels. Also, the FEM results are independent of specimen dimensions; therefore, it is much more reliable than other methods and provide useful measures of the intrinsic fracture toughness of the NiAl/V microlaminates, which would otherwise be very difficult to obtain due to the excessively large specimen dimensions.

100 μm specimen				200 μm specimen				400 μm specimen			
Δa	P_{ex}	P_{FEM}	Error (%)	Δa	P_{ex}	P_{FEM}	Error (%)	Δa	P_{ex}	P_{FEM}	Error (%)
500	860	840	-2.3	1200	950	980	3.2	910	1250	1320	5.6
1090	910	940	3.3	2200	1125	1200	6.7				
1700	980	1080	10.2	4500	1070	1250	16.8				
3040	1025	1240	20.9	5030	1060	1100	3.78				
4860	985	997	0.12								
5210	999	981	-1.8								

Table 4.2. Driving forces from experiment and FEM

Δa: Crack increment μm, P_{ex}: Experimental data (lb) from Mingwei Li, P_{FEM}: FEM prediction (lb)

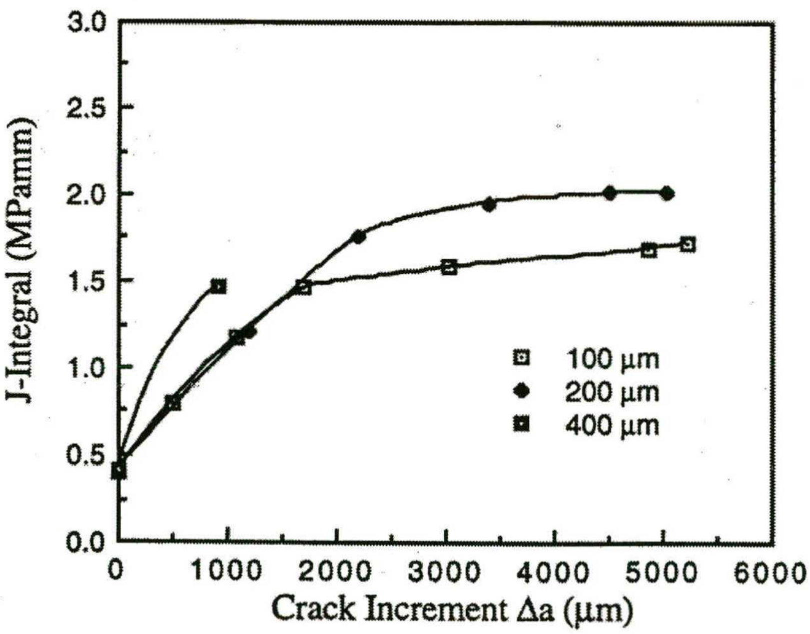

Figure 4.10

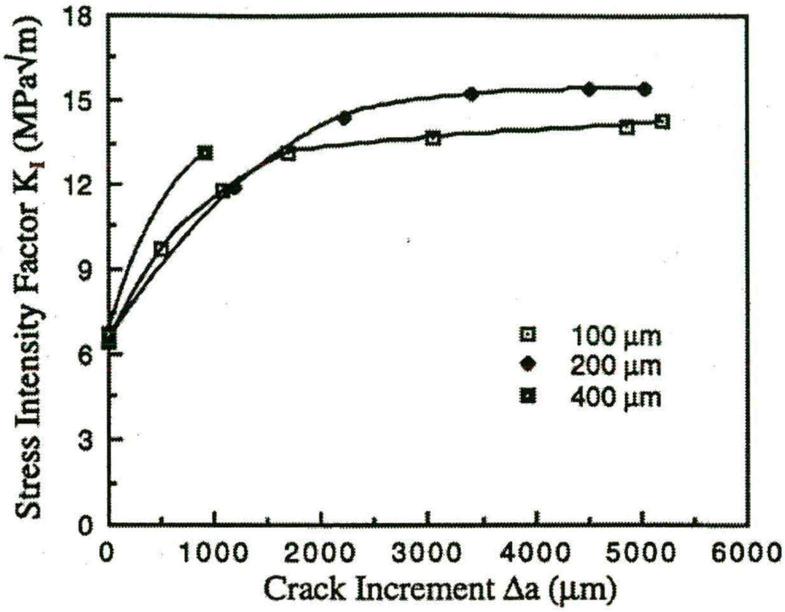

Stress Intensity Factor K_I (MPa√m)
18
15
12
9
6
3
0
0
1000
2000
3000
4000
5000
6000
Crack Increment Δa (μm)
100 μm
200 μm
400 μm

Figure 4.11

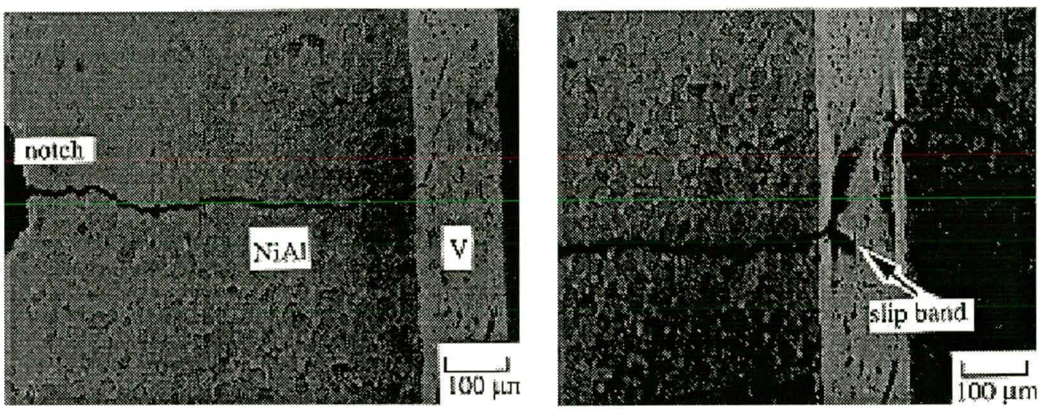

Figure 4.12 Crack propagation in NiAl/V composites: (a) Retardation of the crack and formation of the slip band, and (b) re-initiation of the crack

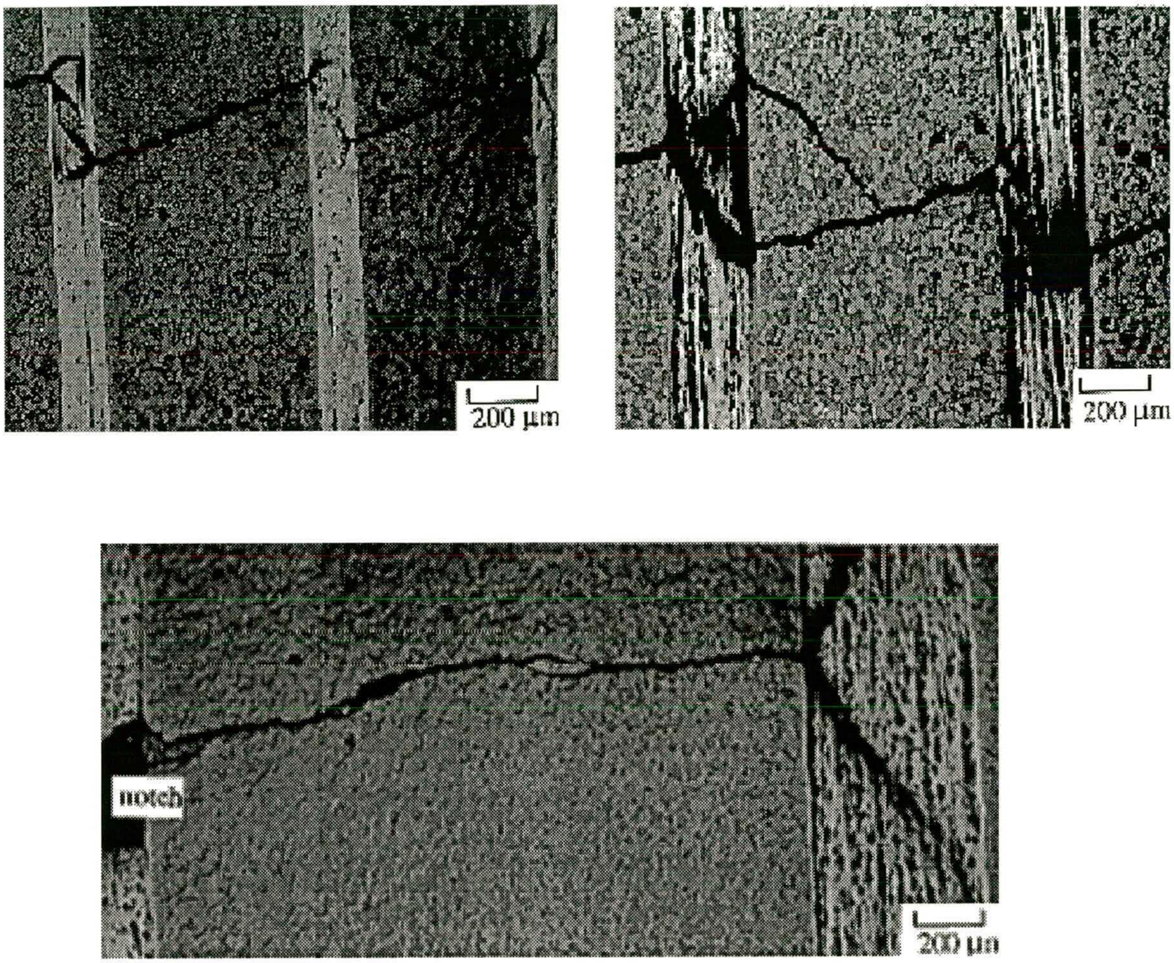

Figure 4.13 Crack/microstructure interactions in NiAl/V composites reinforced with (a)100 μm think vanadium layer, (b) 200 μm think vanadium layer, and (c) 400 μm think vanadium layer

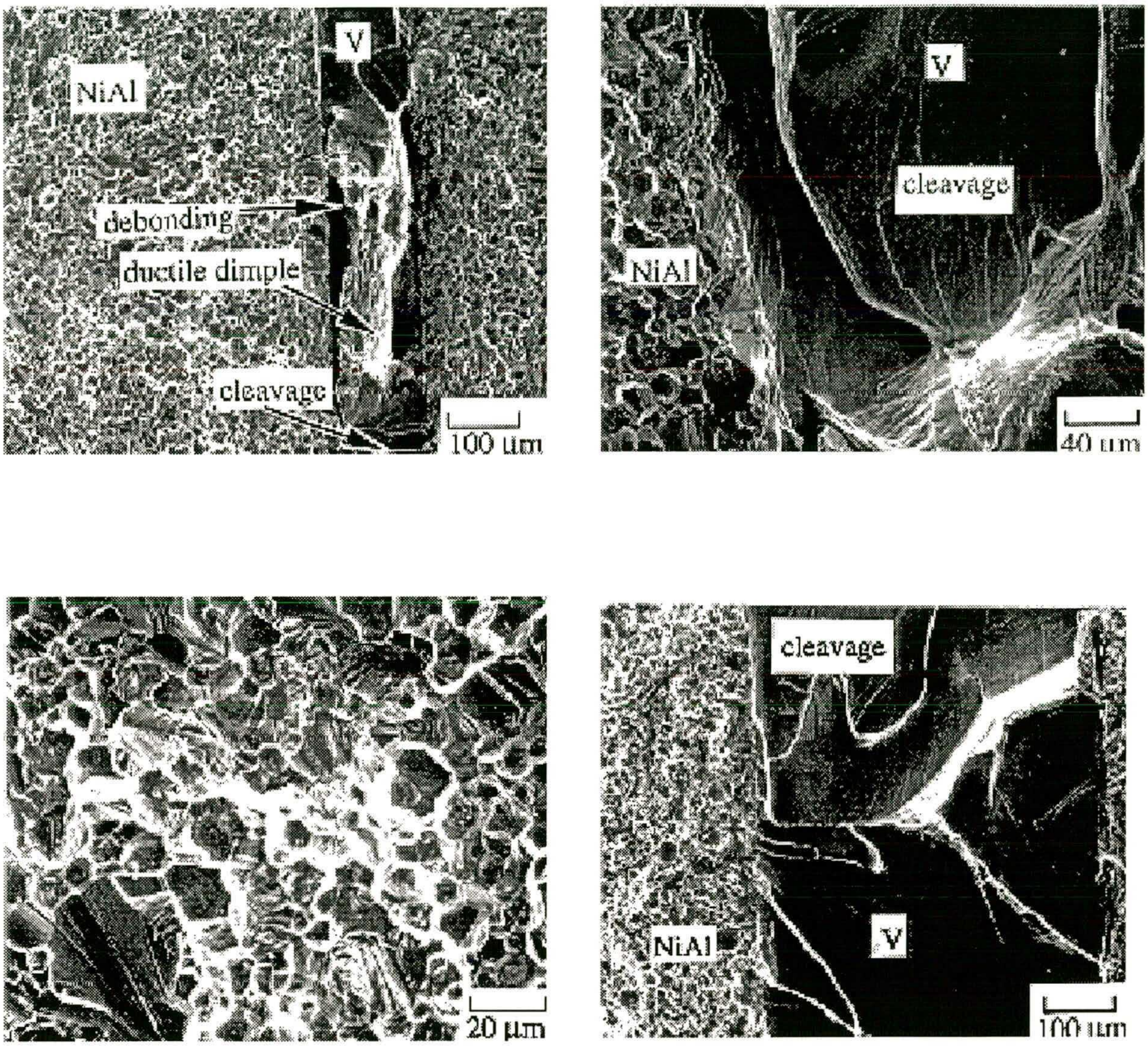

Figure 4.14 Crack/microstructure interactions in NiAl/V composites reinforced with (a)100 µm think vanadium layer, (b) 200 µm think vanadium layer, and (c) 400 µm think vanadium layer

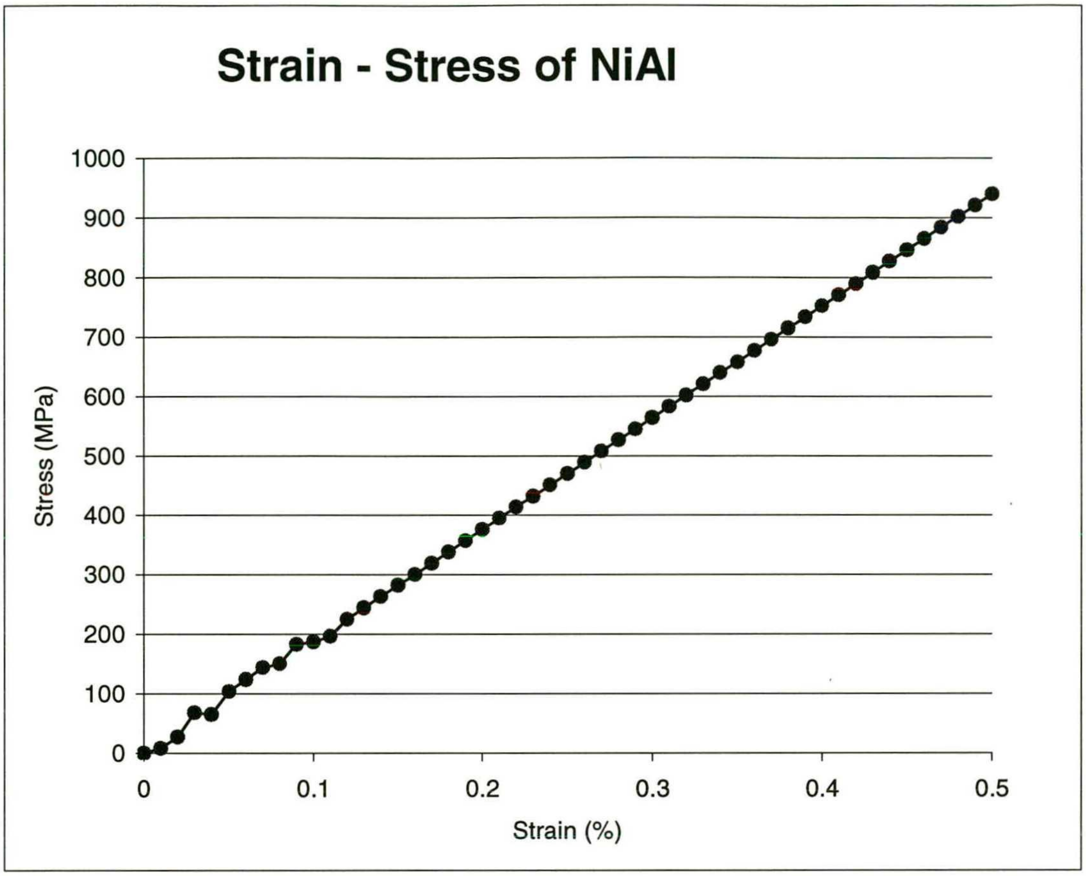

Figure 4.15 Uni-axial Tension Test of NiAl

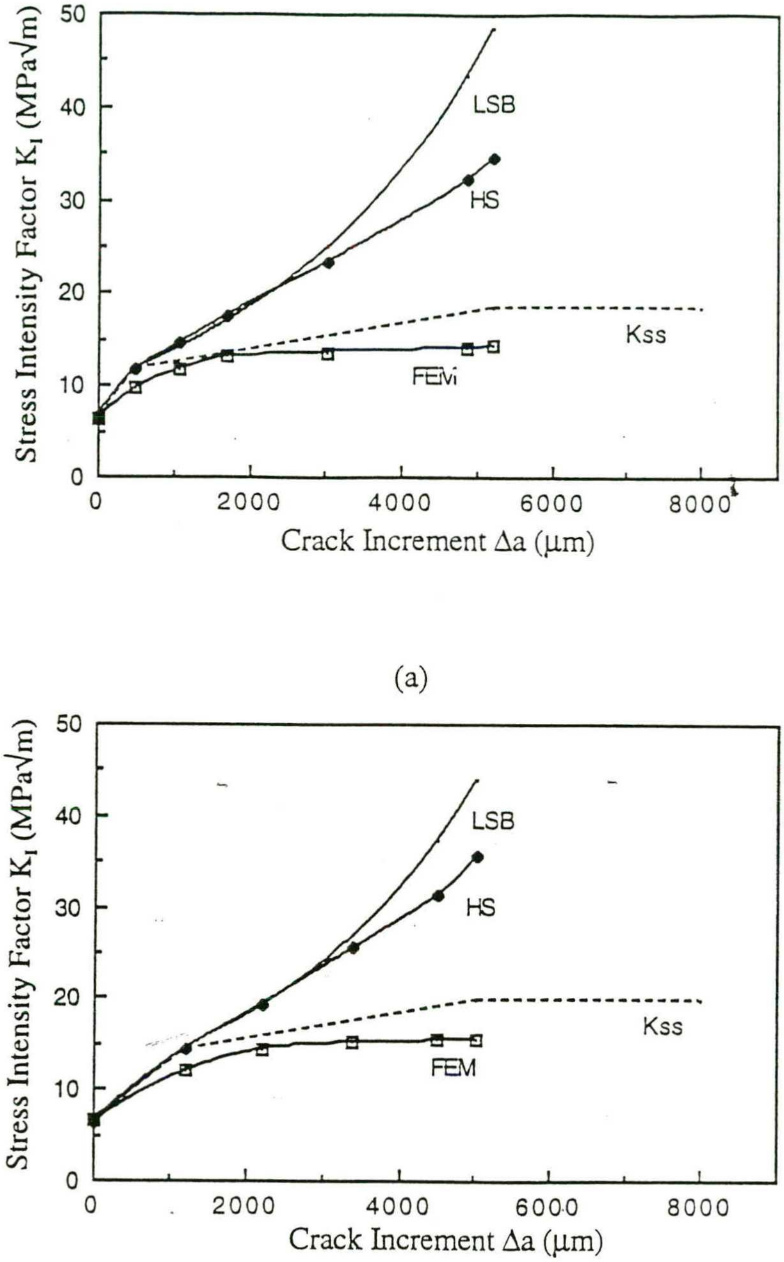

(a)

(b)

Fig. 4.16 Resistance-curve estimated from finite element method(FEM), handbook solutions (HS), and large-scale bridging model (LSB): (a) 100 μm and (b)200 μm vanadium laminates. Kss is the steady-state toughness extracted from the weight function method

CHAPTER 5

CONCLUDING REMARKS

Crack/microstructure interactions have been studied in a layered $MoSi_2$/Nb composite. The studies reveal that the crack/microstructure interactions give rise to shielding due to crack-tip blunting and crack bridging. The numerical result of $K_I = 16.6$ MPa$\sqrt{m}$ is very close to the experimental result.

Finite element models of the observed crack/microstructure interactions were also developed. The models show that the matrix cracks in the $MoSi_2$ are attracted to the softer Nb layers, especially when the cracks are very close to the Nb layers. The driving force for debonding and the mode mixity were found to remain constant with increased debond length.

The fracture behavior of layered NiAl/V composites reinforced with 100, 200 and 400 μm thick vanadium layers has been examined. Similar resistance curve behavior was observed in the composites reinforced with 100 and 200 μm thick vanadium layers. However, the steady-state toughness of the composite with 200 μm thick vanadium layers was found to be greater than that of the composite with 100 μm thick vanadium layers. Also, a somewhat steeper resistance curve was obtained for the composite reinforced with 400 μm thick vanadium layers.

The re-nucleation of cracks in adjacent NiAl layers occurs at positions of maximum shear strain at the interface between NiAl and vanadium. The propagating cracks deviate rapidly back to the mode I direction, as they extend into the NiAl layers.

Toughening and stable crack growth of NiAl/V composites is due largely to crack bridging and crack tip interactions with ductile vanadium layers. Stable resistance curves have been obtained for NiAl/V from finite element method and they provide very useful measures of the intrinsic fracture toughness for excessively large specimen dimensions.

CHAPTER 6

SUGGESTIONS FOR FUTURE WORK

1. The combination of the material toughening and particle transformation behavior should be studied.
2. To decrease the computation time and space requirement for the computer, the distribution and parallel computing method should be better introduced and implemented in finite element analysis. The most time and memory consuming part of the finite element method is to construct, store and solve the stiff matrix, and normally the Gauss elimination method is used to solve the linear equations. If the matrix were partitioned between different processors or different computers, each processor and computer would only store the data which belonged to itself, after the sparse linear equations were solved by iterative method (parallel Gauss-Sideal method, SOR or conjugate gradient method) or direct method (parallel Gauss method) , it would send out the data and boundary conditions to other processors or computers. Using this technique, a very large system could be solved very quickly.
3. The object oriented finite element method should be a topic for future study. Each element would be considered as an object with the information belonging to it, such as material property, number of nodes, strain and stress components. Using the heritage and message hiding technology, efficient and reliable finite element programs could be composed together with the objects made previously. The

application of object-oriented design to the finite element method has several advantages. The primary advantage is that it encourages the developer to abstract out the essential immutable qualities of the components of the finite element method. This abstraction forms the definitions of objects that become the building blocks of the software. The class definitions encapsulate both the data and operations on the data, and provide an enforceable interface by which other components of the software may communicate with the object. Once specified, the object interfaces are frozen. For example, if we have a special element, such as crack tip element to catch the crack tip stress singularity, and we also have other regular elements or other special elements for different purpose, we must first abstract the information about the elements into the two kinds: the information that uniquely belongs to the element itself and should and need not to be seen and modified by other elements; and the information that other elements need, i.e., the interface. The encapsulated information could include shape functions and stress, strain distributions; the interface would include the number of nodes in the element, the coordinates of the elements, the nodal displacements and nodal forces. Thus, the design forms a stable base that can be extended with minimum effort to suit a new task. If a new element, i.e. a new class will be introduced in the future, it could be derived from the existing element and by adding new features or made some modification to the encapsulated information. As the encapsulated information is independent of other elements, any modification to it would not change the encapsulated information belonging to other elements or the structure of the program. But we have to keep the interface frozen so that the other elements will recognize and cooperate with the new element. Due to the encapsulation enforcement inherent in object-oriented languages, new code will work seamlessly with old code to form a new stiff matrix according to the interface the new element provides and get the results. However, to implement the object oriented method, a good design in the beginning is very crucial and much effort would be required because the design would very difficult to be modified with the time being.

LIST OF REFERENCES

1. Ewalds, H, L., Fracture Mechanics, Edward Arnold Ltd. (1984).

2. Irwin, G. R., "Fracture Dynamics," *Fracturing of Metals*, American Society for Metals, Cleveland, OH, pp. 147-166 (1948)

3. Irwin, G. R., "Analysis of Stresses and Strains Near the End of a Crack Traversing a Plate," *Journal of Applied Mechanics*, 24, pp. 361-364 (1957).

4. Kanninen, M. F. and Popelar, C. H., Advanced Fracture Mechanics, Oxford University Press (1985).

5. Rice, J. R., "A Path Independent Integral and the Appropriate Analysis of Strain Concentrations by Notches and Cracks, *Journal of Applied Mechanics*, 35, pp. 379-386 (1968).

6. M. Aindow, J. Shyue, T.A. Gaspar and H.L. Fraser, 1991, Phil. Mag. Lett., Vol. 64, p.59.

7. ASM metals reference book, 1981, American Society for Metals, Metals Park, OH.

8. B. Budiansky, J. W. Hutchinson and J. C. Lambropoulos, 1983, Int. J. Solids Structure, 19 337.

9. H.R. Gray and C.A. Ginty, 1991, "An Overview of NASA's Advanced High Temperature Engine Materials Technology Program," Proceedings of the 4th Annual HITEMP Review, NASA-Lewis Research Center, pp. 1.K

10. S. Chan, Metall. Trans.,1992, vol. 23A, pp. 183-199.

11. P.J. Meschter, 1992, Metall Trans., Vol. 23A, pp.1763-72.

12. R.O. Ritchie and R.M. Cannon, 1985, Report No. LBL-2-656, Lawrence Berkeley Laboratory, University of California, Berkeley, CA.

13. W.O. Soboyejo, F. Ye, L-C. Chen, N. Bahtishi, D.S. Schwartz and R.J. Lederich, 1996, "Investigation of the Effects of Reinforcement Architecture on the Fatigue and

Fracture Behavior of MoSi2/Nb Composites', Acta Metallurgica et Materialia, Vol 44, pp. 207-2041.

14. W.O. Soboyejo, P.B. Aswath and L. Xu, 1997, "Microstructure and the fracture behavior of a Ti-24Al-11Nb Intermetallic", Journal of Materials Science. .
15. S. Suresh and J.R. Brockenbrough, 1988, Acta Metall. Mater. Vol. 36, pp.1444-1470.

16. A. K. Vasudevan and J.J. Petrovic, 1992, Mater. Sci Eng.A, Vol. 155, pp.1-17.

17. J. Zhang, 1995, "A Hybrid Finite Element Method for Heterogeneous Media with Random Microstructures", Ph.D. Dissertation, The Ohio State University.

18. R. Wang and F. Ye et al., "The effect of layer thickness on crack propagation", ASME 1997.

19. R. Wang and M. Li et al. "An Finite Element Analysis of the Fracture Behavior of Layered NiAl/V Composites" PACM-VI, 1999.

20. M. Li and R. Wang et al. "An Investigation of Fracture Behavior in Layered NiAl/V Composites" Acta Materialia 1998.

21. M. Li and R. Wang et al., "An Investigation of the Effects of Layer Thickness on the Fracture Behavior in Layered NiAl/V Composites" , Mechanical Behavior of Advanced Materials, ASME 1998.

22. ABAQUS manual, Hibbitt, Karlsson & Sorensen, Inc., Pawtucket, RI

23. Standard test method for plane-strain fracture toughness of metallic materials, Annual Book of ASTM Standard, Part 10, E399-81, American Society for Testing and Materials, Philadelphia, pp.592-621 (1981).